



An Experimental Investigation of a Wing-Fuselage Junction Model in the NASA Langley 14- by 22-Foot Subsonic Wind Tunnel

Michael A. Kegerise*, Dan H. Neuhart†, Judith A. Hannon‡, and Christopher L. Rumsey§

NASA Langley Research Center, Hampton, VA 23681

Current turbulence models, such as those employed in Reynolds-averaged Navier-Stokes CFD, are unable to reliably predict the onset and extent of the three-dimensional separated flow that typically occurs in wing-fuselage junctions. To critically assess, as well as to improve upon, existing turbulence models, experimental validation-quality flow-field data in the junction region is needed. In this paper, we present an overview of experimental measurements on a wing-fuselage junction model that addresses this need. The experimental measurements were performed in the NASA Langley 14- by 22-Foot Subsonic Tunnel. The model was a full-span wing-fuselage body that was configured with truncated DLR-F6 wings, both with and without leading-edge extensions at the wing root. The model was tested at a fixed chord Reynolds number of 2.4 million, and angles-of-attack ranging from -10 degrees to +10 degrees were considered. Flow-field measurements were performed with a pair of miniature laser Doppler velocimetry (LDV) probes that were housed inside the model and attached to three-axis traverse systems. One LDV probe was used to measure the separated flow field in the trailing-edge junction region. The other LDV probe was alternately used to measure the flow field in the leading-edge region of the wing and to measure the incoming fuselage boundary layer well upstream of the leading edge. Both LDV probes provided measurements from which all three mean velocity components, all six independent components of the Reynolds-stress tensor, and all ten independent components of the velocity triple products were calculated. In addition to the flow-field measurements, static and dynamic pressures were measured at selected locations on the wings and fuselage of the model, infrared imaging was used to characterize boundary-layer transition, and oil-flow visualization was used to visualize the separated flow in the leading- and trailing-edge regions of the wing. Sample results from the measurement techniques employed during the test are presented and discussed.

Nomenclature

<i>c</i>	chord length at wing planform break
<i>f</i>	frequency or focal length
<i>i</i>	<i>i</i> th sample
<i>ℓ</i>	length of the corner-flow separation
<i>N</i>	number of samples
<i>p'</i>	fluctuating pressure
<i>q</i> _∞	freestream dynamic pressure, $q_{\infty} = \rho_{\infty} U_{\infty}^2 / 2$
<i>Re</i> _c	Reynolds number based on chord length at wing planform break
<i>Re</i> _s	Reynolds number based on distance along the surface
RMS	root-mean-squared value
<i>u</i>	<i>x</i> component of velocity
<i>U</i> _ℓ	uncertainty in the corner-flow separation length measurement
<i>U</i> _w	uncertainty in the corner-flow separation width measurement
<i>u</i> _τ	friction velocity
<i>U</i> _∞	freestream velocity
<i>v</i>	<i>y</i> component of velocity

*Research Scientist, Flow Physics and Control Branch, M.S. 170

†Research Scientist, Flow Physics and Control Branch, M.S. 170.

‡Aerospace Engineer, Flow Physics and Control Branch, M.S. 170.

§Research Scientist, Computational Aerosciences Branch, M.S. 120. Fellow AIAA.

w	z component of velocity or width of corner-flow separation
x	distance along length of model from nose tip
y	distance towards starboard wing tip from model nose tip
y_o	y location of the fuselage surface
y^+	y location in wall units
z	distance above model nose tip
z_o	z location of the wing surface
α	geometric model pitch angle
ν	kinematic viscosity
ρ_∞	freestream density
τ_i	particle transit time through measurement volume for the i th sample
$(\bar{\ })$	mean value
$(\)'$	fluctuating value

I. Introduction

Junction flows, such as those formed around a wing-fuselage or a wing-pylon intersection, are common features of practically all civil and military aircraft. Since these flows typically exhibit regions of flow separation that can adversely impact aircraft performance, there is a strong desire to accurately predict the behavior associated with them. For wing-fuselage junction flows in particular, the flow is often observed to separate in the corner-flow region near the wing trailing edge. However, the turbulence models currently employed in Reynolds-averaged Navier-Stokes CFD are unable to reliably predict the onset and extent of this separated corner flow. For example, CFD computations at past Drag Prediction Workshops have displayed large variations in the predictions of separation, skin friction, and pressure in the corner-flow region near the wing trailing edge.¹ To critically assess our existing turbulence models, as well as to improve upon them, experimental validation-quality flow-field data in the junction region is needed. To address that, NASA has developed a CFD validation experiment for a generic full-span wing-fuselage junction model at subsonic conditions. Rumsey *et al.* have previously reported on the detailed goals of this effort and has provided a history of its development.^{2,3} The ultimate goal of this experiment is to provide a publicly-available high-quality flow field and surface data set with quantified boundary conditions, geometry, and measurement uncertainties. This data set should be suitable for use in CFD workshop environments and will help CFD practitioners validate and improve their predictive capabilities for turbulent separated corner flows.

Initially, a full-span wing-fuselage body with top-bottom/left-right symmetry and a symmetric-wing profile was desired for the junction flow CFD validation experiment. That would allow us to make measurements with the model both upright and inverted so that geometric imperfections in the model and flow nonuniformities in the freestream would be exposed, and their impact on measurement uncertainty could be assessed.^{4,5} Furthermore, we hoped that such a configuration would display fully-attached corner flow, incipient corner-flow separation, and a large corner-flow separation simply by varying the freestream Mach number or the model pitch angle. Several symmetric-wing profiles and a cambered-wing profile (the DLR-F6) were analyzed via CFD, but none of them displayed all of the desired flow-separation conditions.² However, given the current limitations of the CFD turbulence models for separated flows, and our lack of trust in them, we decided to perform a couple of risk-reduction experiments on flow-visualization models to see whether or not corner-flow separation occurred in the trailing-edge region and if it did, to document its progression with model pitch angle.^{2,6,7} In these risk-reduction experiments, full-span wing-fuselage junction models with five interchangeable wing designs were considered, and oil-flow visualizations were used to document the surface topology in the corner-flow region. All of the wing configurations, except for a design based on an NACA 0015 wing, indicated corner-flow separation for all of the model pitch angles considered (-10° to 10°). In contrast, the NACA 0015 wing indicated a progression from fully attached flow to separated corner-flow for the range of pitch angles considered, but the separated-flow region remained very small in size.

While the NACA 0015 wing design did provide the desired progression from attached flow to separated flow, the small extent of the corner-flow separation would be hard to probe experimentally and still achieve the desired spatial resolution. On the other hand, a design based on the DLR-F6 wing did provide a progression from a small corner-flow separation to a large one that could be easily probed for flow-field measurements. Of course, the down side of the DLR-F6 wing was the loss of symmetry in the wing profile and with that, the ability to fully probe uncertainties due to geometric imperfections. Since neither wing design was optimal in terms of our original requirements, a decision was made to design and build both wings for the CFD validation experiment.

In late 2017 and early 2018, the junction flow CFD validation experiment was conducted in the NASA Langley 14- by 22-Foot Subsonic Tunnel (14x22) and in this paper, we provide an initial report out on that test entry. The primary objective of this first test entry was to perform flow-field measurements in the trailing-edge corner region of the wing-fuselage junction model using an internally mounted laser Doppler velocimetry (LDV) system. For this set of measurements, the junction model was configured with the DLR-F6 wing geometry. The LDV system provided measurements from which of all three velocity components, all six independent components of the Reynolds-stress tensor, and all ten independent components of the velocity triple products were calculated. A second internally mounted LDV system was alternately used to measure the flow field in the leading-edge region of the wing and to measure the incoming fuselage boundary layer well upstream of the leading edge. In addition to the flow-field measurements, static and dynamic pressures were measured at selected locations on the wings and fuselage of the model, infrared imaging was used to characterize boundary-layer transition, and oil flow was used to visualize the separated flow in the leading- and trailing-edge regions of the wing. Sample results from these measurement techniques will be presented and discussed in this paper (with the exception of the static pressure results, which will be reported at a later time).

It should be noted that a concerted effort was also made to document the as-built, as-assembled, and as-tested geometry of the junction model using laser-based scanning techniques over the course of the test entry. In addition, the wind-tunnel test-section geometry was documented and measurements of the tunnel wall pressures, diffuser pressures, and boundary-layer rake pressures were acquired as boundary conditions during the test entry. An earlier test entry in the 14- by 22-Foot Subsonic Tunnel also attempted to characterize the test-section inflow using various measurement techniques.⁸ The ultimate goal for this group of measurements is to provide documented boundary conditions and geometry so that an unambiguous comparison between CFD calculations and the experimental measurements can be made. These aspects of the junction flow CFD validation experiment are not included in this paper and will be documented at a later date.

In the next section, the experimental methods are presented, and details of the wind-tunnel facility and the junction model are provided, along with the details of the model instrumentation. Sample results for the experimental measurements are then presented and discussed, followed by a summary of the paper.

II. Experimental Methods

A. Wind-Tunnel Facility

The experiment was performed in the NASA Langley 14- by 22-Foot Subsonic Tunnel, which is a closed-circuit, atmospheric-pressure wind tunnel capable of operating in an open, partially closed, or closed test-section mode. Raising and lowering the north and south walls and ceiling creates the various modes of tunnel geometry. The floor of the test section is formed by two model carts that are moved to and from the test section front and back bays. The carts are raised and lowered on hydraulic lifts and transported along the floor under the test section on air pads. Once in place, the tunnel floor is fixed during testing. Measurements for this test were made in the closed test-section mode. In that mode, the test section measures 4.42 m high and 6.63 m wide, and the maximum free-stream velocity is 103 m/s. Flow conditioning is provided by a flow-straightening honeycomb, four square-mesh screens with a mesh count of 10 per inch and 64% open area, and a tunnel contraction ratio of 9 to 1. This arrangement achieves a low test-section turbulence intensity of between 0.07 and 0.08 percent at a dynamic pressure (q_∞) of 2.87 kPa (60 psf)—but that does vary somewhat with dynamic pressure and location in the test section.⁹ Further details about the tunnel can be found in Gentry *et al.*¹⁰

Several key tunnel parameters were monitored and measured during a wind-tunnel run. The total pressure was measured downstream of the mesh screens with a silicon pressure transducer (SPT) and the differential pressure between the total pressure and the static pressure at the test-section entrance was also measured with an SPT. The air temperature and the dew-point temperature—both of which were measured at the test-section entrance—were measured with a 4-wire RTD and a dew-point hygrometer, respectively. Using these four parameters, all other test conditions were calculated according to the equations documented by Boney.¹¹

Throughout all of the wind-tunnel runs, the tunnel controller held the chord Reynolds number, Re_c , at a constant value of 2.4 million. Since the facility does not have a temperature controller, the air temperature increased over the course of a given run and therefore, the velocity was increased accordingly to maintain a constant chord Reynolds number. In addition, there were substantial changes in the nominal air temperature from day-to-day and over the course of the test entry due to prevailing outdoor conditions. As such, the nominal tunnel velocity was again adjusted to maintain the target chord Reynolds number. In general, the air temperature ranged from 275 to 308 K and the Mach number ranged from 0.175 to 0.205 over the course of the test entry.

B. Wing-Fuselage Junction Model

The model was a full-span wing-fuselage body fabricated from 6061-T6 aluminum. The overall length, height, and width of the fuselage was 4.839 m, 0.670 m, and 0.472 m, respectively, and the tip-to-tip wing span was 3.397 m. A port-side view of the model installed in the 14x22 wind tunnel is shown in Fig. 1 and CAD drawings showing the top, front and port-side views of the junction-model assembly are shown in Figs. 2–4. The model was painted with a black lusterless polyurethane paint suitable for both infrared imaging and oil-flow visualizations on the model surface. A coating thickness gauge, which uses eddy-current principles to measure the coating thickness on non-ferrous metals, indicated a paint thickness on the order of 254 to 330 μm (10–13 mils).

The model was attached to a long sting that could be raised or lowered via a motorized sting mast to keep a reference point on the model near the center of the test section during a pitch-angle adjustment. The reference point was located 2.448 m from the model nose tip (5.41 m from the test-section entrance) and on the fuselage centerline. Pitch angles for this test ranged from -10° to 10° in increments of 2.5° . Generally, the nominal height of the reference point was 2.2098 m above the test-section floor; however, for pitch angles of -10° and -7.5° , that height could not be achieved due to geometrical constraints on the sting-mast height. As such, the height was reduced to 1.7907 m and 2.0574 m, respectively, for those two angles. The model sting was also motorized to allow for adjustments of the model roll angle, and over the course of this test, roll angles of 0° and 180° were considered. The pitch and roll angles of the model were measured with a pair of accelerometer-based model-attitude sensors that were located inside the model fuselage, and both sensors had a measurement uncertainty of $\pm 0.01^\circ$. To quantify vibration levels during a wind-tunnel run, the junction model was instrumented with accelerometers to measure three orthogonal components of acceleration. These sensors were mounted inside the model to a fixture on the wing box.

The junction-model fuselage was built in two parts: the fuselage nose section and the fuselage main section. An exploded view of the fuselage nose-section assembly is shown in Fig. 5a. The port and starboard sides of the fuselage nose section were designed to be flat so that flat instrumentation inserts could be used. The inserts were centered on the model centerline and 1168.4 mm from the nose-section tip. Different types of insert plates were used, depending on the objectives of a given run. For the LDV measurements, the insert had an acrylic window. Other inserts were made for an unsteady pressure transducer, a Preston tube, and an array of static-pressure ports. Removable hatches on the top and bottom of the fuselage nose section provided internal access to the instrumentation. In Fig. 5b, a CAD drawing of the port side of the fuselage nose section is shown with an LDV/traverse assembly in place. This assembly was mounted to a bridge piece located inside the nose section.

An exploded view of the fuselage main section is shown in Fig. 6. This section has four removable inserts that were located on the flat sections of the fuselage sidewalls. On the port side, one insert was located upstream of the wing box, providing access to the leading-edge region of the wing. The other insert was located downstream of the wing box, providing access to the trailing-edge region of the wing. These inserts were mirrored on the starboard side of the fuselage main section. As with the fuselage nose section, several types of insert plates were used. Acrylic window inserts were used on the port side of the model to provide optical access for the LDV measurements. Solid inserts with static pressure ports were also used on this side of the model. On the starboard side of the model, both inserts were instrumented with static pressure ports and unsteady pressure transducers. A large removable hatch on the top side of the fuselage main section and two smaller hatches on the bottom provided internal access to the instrumentation. Cabling for the instrumentation was routed through the model sting and through four PVC conduits arranged around the sting adaptor at the back end of the fuselage. Cables routed through the conduits were secured to the model sting and sting mast with duct tape and zip ties. In Fig. 6, the fuselage main section is shown with two LDV/traverse assemblies in place and these assemblies were mounted to bridge pieces located inside the main section.

The junction model was configured with truncated DLR-F6 wings that are characterized by a leading-edge sweep angle of 27.1° , dihedral, wash-out twist toward the wing tip, and a planform break located 759 mm from the fuselage side wall. The planform break chord length for the wings was 557.17 mm and this was used as the reference



Figure 1. Port-side image of the wing-fuselage junction model installed in the 14- by 22-Foot Subsonic Tunnel.

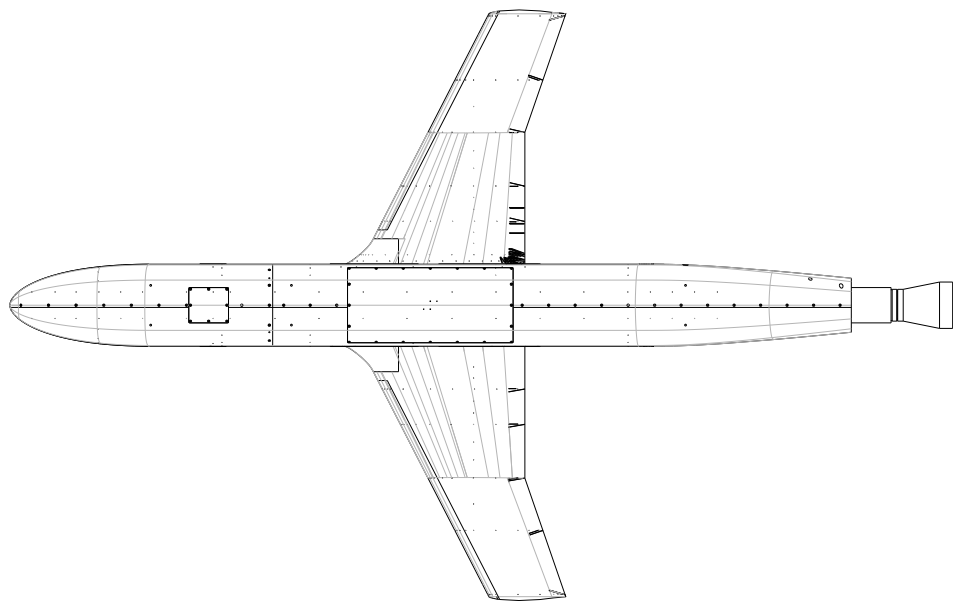


Figure 2. Top view of the wing-fuselage junction model assembly.

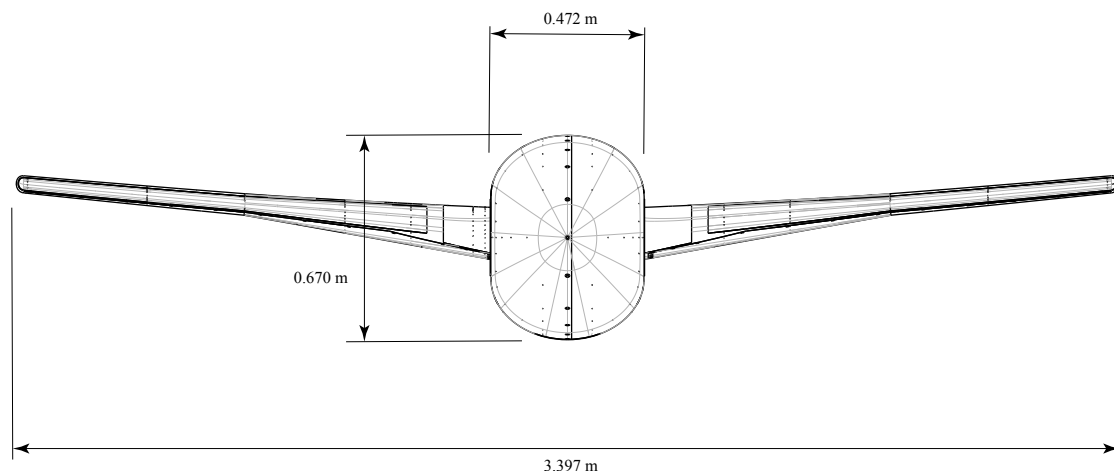


Figure 3. Front view of the wing-fuselage junction model assembly.

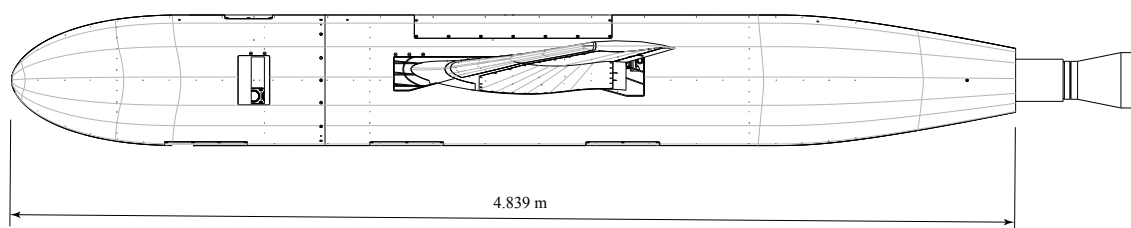
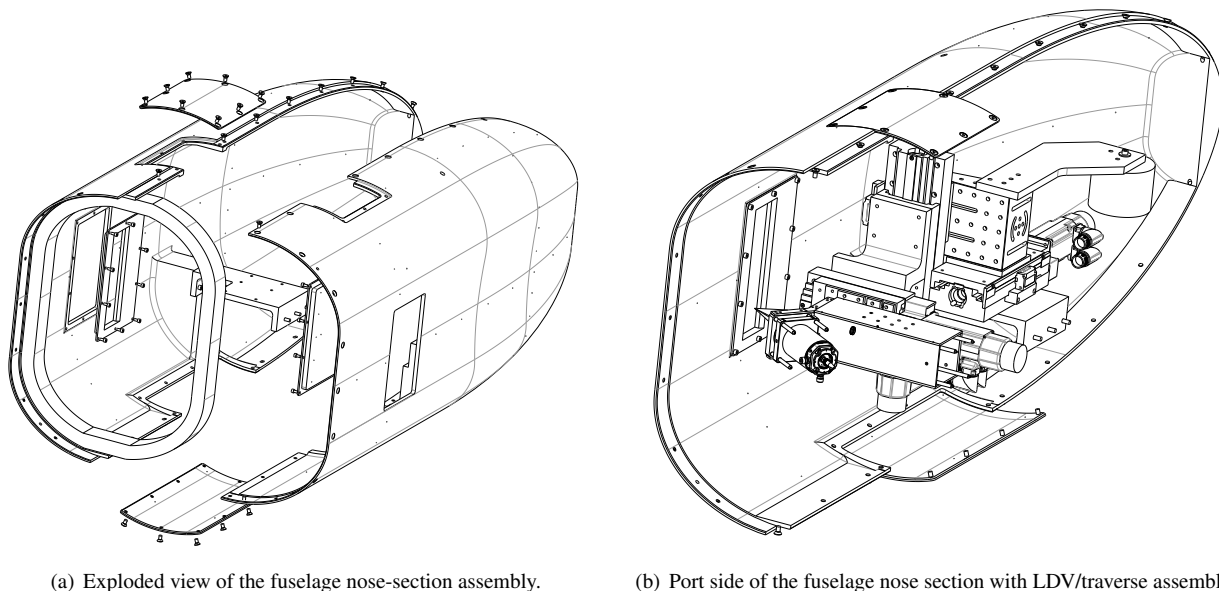
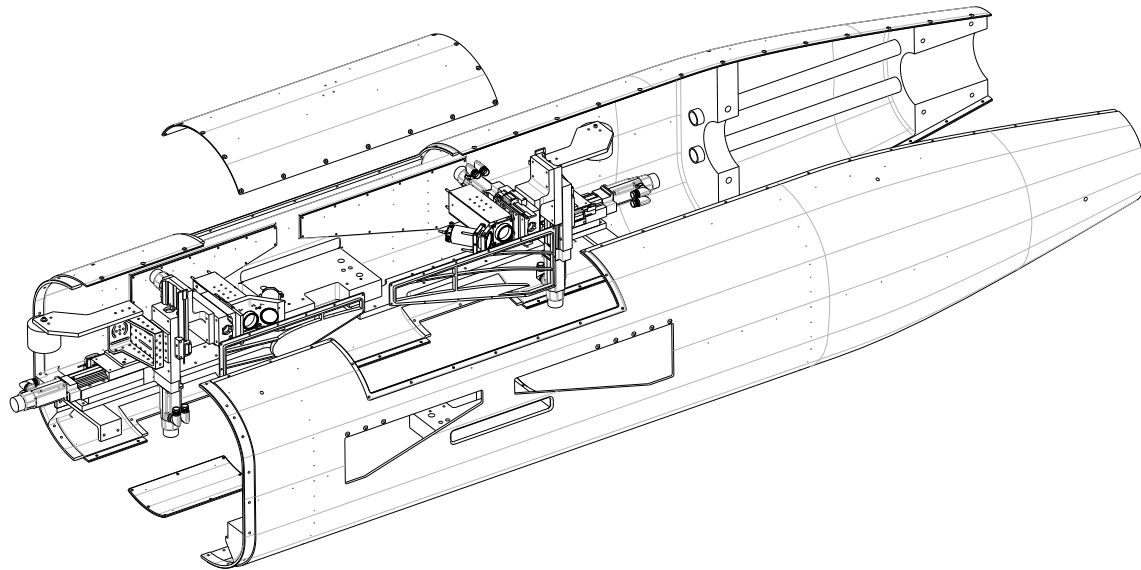


Figure 4. Port-side view of the wing-fuselage junction model assembly.



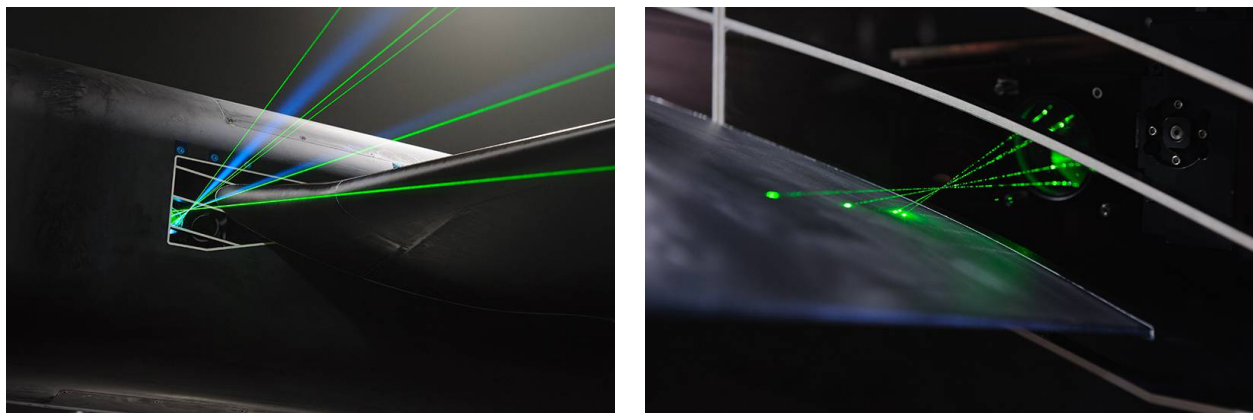
(a) Exploded view of the fuselage nose-section assembly.

(b) Port side of the fuselage nose section with LDV/traverse assembly.

Figure 5. CAD drawings of the fuselage nose section.**Figure 6. Exploded view of the fuselage main section assembly.**

length when calculating the chord Reynolds number. Using a removable insert around the leading-edge root region of the wing, the F6 wing could be configured with or without a leading-edge extension. This extension is simply a geometrical fairing intended to eliminate or minimize the development and influence of the horseshoe vortex that normally forms at the wing leading edge in the absence of the extension. A top view of the wing planform with the leading-edge extension can be seen in Fig. 2. Both port and starboard wings were instrumented with static pressure ports and the starboard wing was additionally instrumented with unsteady pressure transducers. Further details on that instrumentation will be provided in a subsequent section.

To ensure a turbulent boundary layer on the fuselage and the upper and lower surfaces of the wing, trip-dot arrays were used to fix the transition location. The trip dots were applied to the model with a commercially-produced trip-dot tape that is available in a range of heights. Specific details for the trip-dot placement on the fuselage and wings,



(a) LDV system located near the wing leading edge.

(b) LDV system located near the wing trailing edge.

Figure 7. Images of the LDV systems installed at the leading- and trailing-edges of the junction model.

including trip-dot geometry, will be presented in the Results section below.

C. Laser Doppler Velocimetry Measurements

As indicated in the previous section, a pair of miniature laser Doppler velocimetry (LDV) probes were located inside the model and each one was mounted to a three-axis traverse system. The LDV probes provided flow-field measurements yielding all three velocity components, all six independent components of Reynolds stress, and all ten independent components of the velocity triple products. In addition, each probe had the capability to measure the particle position within the measurement volume and that feature could be used to achieve submeasurement-volume spatial resolution. During the test entry, both LDV probes were operated simultaneously and measurements were made only on the port side of the model. One probe was located near the trailing-edge of the wing and was used to measure upstream of and inside the separated corner flow. The other probe was alternately used to measure the flow field in the leading-edge region of the wing and to measure the incoming boundary layer on the fuselage nose section. Images of the LDV systems installed at the leading-edge and the trailing-edge of the port wing are shown in Figs. 7a and 7b.

Each LDV system consisted of a photonics system that provided laser light to the LDV probe, a fiber-optic based probe head with off-axis receiving optics, a set of photomultipliers to detect Doppler bursts, and a data-acquisition computer with a high-speed A/D board and software for burst processing.^a The photonics system, which resided in a cart located outside the test section, consisted of the laser systems, discrete optics, and acousto-optical modulators (Bragg cells). Laser light for the system was provided by three continuous-wave diode-pumped solid-state lasers with a power output of 1 W. Lasers 1 and 2 provided laser light with a wavelength of 532 nm (green) and laser 3 provided laser light with a wavelength of 488 nm (blue). Laser 1 was used to produce two beams (beam 1 with a frequency shift of 0 MHz and beam 2 with a frequency shift of -200 MHz) that were delivered to the probe head via polarization-maintaining (PM) fibers. Laser 2 was used to produce three beams (beam 3 with a frequency shift of 0 MHz, beam 4 with a frequency shift of -80 MHz, and beam 5 with a frequency shift of 350 MHz) that were delivered to the probe head via PM fibers. Laser 3 was used to produce two beams (beam 6 with a frequency shift of 0 MHz and beam 7 with a frequency shift of -200 MHz) that were also delivered to the probe head via PM fibers. All seven single-mode PM fibers were bundled together in a stainless-steel armored conduit that was run from the photonics cart to the probe head in the junction model.

The LDV probe head, which is shown in Fig. 8, was 22.8 cm long by 8 cm high by 7.7 cm wide. Laser light emitted from each of the PM fibers was collimated by a set of aspheric lenses that were arranged with the pattern shown in Fig. 9. The beams emitted from the collimating lenses were then focused by a 90 mm focal length transmitting lens to form four overlapping measurement volumes. The power of the laser beams emitted from the probe head were typically on the order of 100 mW for beams 1–5 and 150 mW for beams 6 and 7.

The five green (532 nm) laser beams (beams 1–5) emitted from the probe head were crossed at their beam waists to form three measurement volumes: beams 1 and 2 with a frequency shift of -200 MHz, beams 3 and 4 with a frequency shift of -80 MHz, and beams 3 and 5 with a frequency shift of 350 MHz. Note that an additional measurement volume

^aThe LDV system used in our study was a custom design delivered by Applied University Research, Inc. under a Phase III SBIR contract (80NSSC18P0088).

was formed due to the interference between beams 4 and 5 and has a frequency shift of 430 MHz. However, the burst signals from this measurement volume are redundant and were discarded during the processing steps. The optical frequency shift of one beam relative to the other in each measurement volume was used to set up traveling interference fringes that can be used to determine the direction of particle motion.¹² For each of the three measurement volumes mentioned above, the nominal diameter and length of the measurement volume was 140 μm and 960 μm , respectively. The measurement directions defined by these three measurement volumes are nonorthogonal and therefore, it was necessary to form a linear transformation to convert the measured velocity components to an orthogonal body-fixed coordinate system.

The two blue (488 nm) laser beams (beams 6 and 7) emitted from the probe head were crossed at the measurement volumes formed by the green laser beams. However, this crossing occurred before the beam waists of the blue beams and that produced a converging set of fringes along the bisector of the two interfering beams.¹³ In other words, the fringe spacing becomes smaller along the length of the measurement volume when moving away from the probe. Using the Doppler frequency measured with this converging fringe pattern and the velocity measured by the conventional green-beam measurement volumes (which have a uniform fringe pattern), the local fringe spacing of the converging fringe volume can be deduced and that in turn yields a measure of the particle position along the length of the measurement volume. Further details on the theory and development of this particle-position-resolving capability can be found in Lowe¹⁴ and in several other references.^{15–17}

Scattered light from particles moving through the measurement volume was collected with a 110 mm focal-length lens oriented at approximately 35° to the optical axis of the probe head. Light collected with that lens was then focused onto a multimode fiber with a diameter of 105 μm . This off-axis arrangement of the receiving optics reduced the effective length of the measurement volume to approximately 180 μm . The multimode receiving fiber was routed out of the junction model and test section to an enclosure that housed two photomultipliers that measured the green light and blue light burst signals carried by

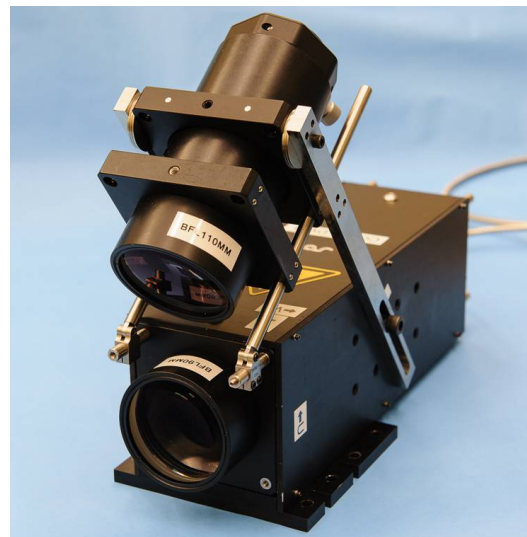


Figure 8. Photograph of the LDV probe head with off-axis receiving optics.

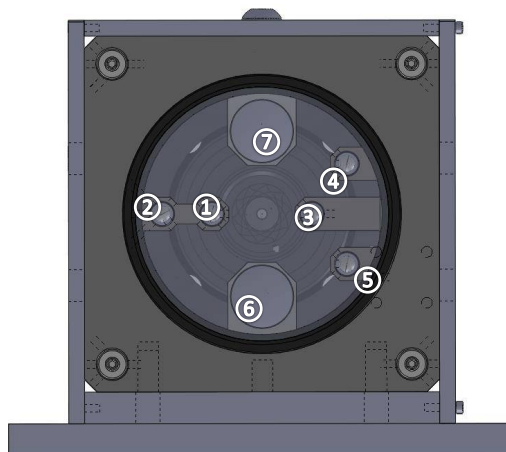


Figure 9. Front view of the LDV probe head with annotated locations for the collimating lenses of the seven laser beams. Beams 1 (0 MHz) and 2 (-200 MHz) were produced by laser 1 (532 nm). Beams 3 (0 MHz), 4 (-80 MHz), and 5 (350 MHz) were produced by laser 2 (532 nm). Beams 6 (0 MHz) and 7 (-200 MHz) were produced by laser 3 (488 nm).

the receiving fiber. The amplified signals from the photomultipliers were then sent to the inputs of an 8 bit, 1 GS/s data-acquisition card.

Burst signals from the LDV system were processed with proprietary software developed by Applied University Research, Inc. For our system, the software was configured to sample the two electronic signals from the photomultipliers. Burst detection for each channel was performed in the time domain and Doppler frequencies were extracted from the power-spectral densities of the sampled burst signals. Details on the burst processing algorithm can be found in Lowe.¹⁴ For the blue channel burst signals, a single Doppler frequency associated with the single measurement volume was present. For the green channel burst signals, three Doppler frequencies, associated with the three measurement volumes, were present. Here, the frequency shift for each measurement volume was separated far enough apart in the frequency domain so that no signal ambiguity could occur for our flow conditions.

Seeding for the LDV measurements was provided by a smoke generator that uses a low-residue mineral oil and produces a narrow distribution of particle sizes with a nominal diameter of $0.94\text{ }\mu\text{m}$. The smoke generator was placed in the wind tunnel settling chamber ahead of the honeycomb and it was necessary to run the generator continuously during a run so that adequate burst data rates could be maintained. Depending on where the measurement volume was located in the flow field, validated burst data rates on the order of 100 burst/s to 500 bursts/s were achieved.

The measurement volume of the LDV probe was positioned in the flow field with a three-axis traverse system. Each stage in this system was of a center-driven leadscrew design where the leadscrews were driven by servo motors. Linear encoders were used to measure the stage positions and to provide feedback to the stage controllers. Traverse motion was performed in a body-fixed coordinate system with origin at the model nose tip and with coordinate directions as shown in Fig. 10. With the model at a pitch angle of 0° for example, the x -coordinate is positive in the downstream direction, the y -coordinate is positive towards the starboard wing tip, and the z -coordinate is positive in the upward direction. The x -axis stage had a travel of 152.4 mm, a positional accuracy of $15\text{ }\mu\text{m}$, and a bidirectional repeatability of $\pm 1\text{ }\mu\text{m}$. The y -axis stage had a travel of 101.6 mm, a positional accuracy of $10\text{ }\mu\text{m}$, and a bidirectional repeatability of $\pm 1\text{ }\mu\text{m}$. The z -axis stage had the same specifications as the x -axis stage.

To locate the LDV measurement volume relative to the fuselage window surface, the measurement volume was scanned through the window in the $-y$ direction at low laser power and the scattered light received at the photomultiplier was recorded. When the measurement volume center was located at the outer surface of the window, the RMS voltage from the photomultiplier peaked and that location was set as the origin for the y axis. A similar procedure was used to locate the measurement volume relative to the wing surface and to set the origin for the z axis. Both window- and wing-surface scans were performed before each flow-field survey. Furthermore, these scans were performed at the desired test condition so that any deflections of the window or wing surfaces were accounted for. To find the x locations for the flow-field measurements, the measurement volume was positioned relative to reference marks on the windows that were at known locations from the model nose tip.

Further details on the LDV system hardware and the traverse system hardware can be found in Kegerise and Neuhart.¹⁸

1. Processing of Laser Doppler Velocimetry Data

To process the LDV data, the unit vectors for each beam emitted by the LDV probe head were first measured using the digital-image-processing methodology described in Kegerise and Neuhart.¹⁸ This was performed each time the LDV probe/traverse assembly was moved to a new location in the model (for example, when moving the assembly from the fuselage nose section to the wing leading edge). Using the measured unit vectors for each pair of beams that form a measurement volume, the measurement direction unit vectors and the measurement volume fringe spacings were calculated. After a fixed number of Doppler bursts were sampled, the measured Doppler frequencies from the three measurement volumes formed by the five green laser beams were used to calculate the nonorthogonal velocity components in the probe optical axes. The histograms of those velocity components were then calculated and the histogram-clipping routine of Ölçmen and Simpson¹⁹ was applied for removal of noise and outliers. The

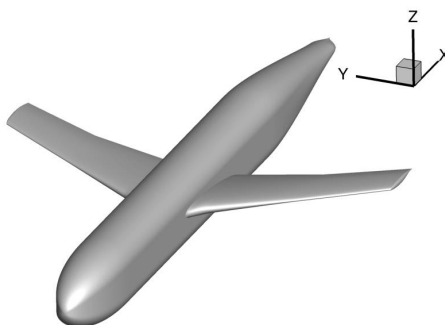


Figure 10. Body-fixed coordinate system for the junction model. The origin of the coordinate system is located at the model nose tip.

Downloaded by NASA LANGLEY RESEARCH CENTRE on January 30, 2019 | http://arc.aiaa.org | DOI: 10.2514/6.2019-0077

velocity components in the probe optical axes were then transformed to orthogonal velocity components in the body-fixed coordinate system. Histograms of those transformed velocity components were calculated and once again, the histogram-clipping routine was applied.

The processed velocity samples—which were sampled with random spacing in time—were then used to calculate several statistical moments. To account for velocity bias effects on the statistical moments, each sample was weighted by the particle transit time through the measurement volume (or burst duration, which was recorded by the burst processor for each sample).¹² With this weighting factor, the mean x component of velocity was calculated as:

$$\bar{u} = \frac{\sum_i^N u_i \tau_i}{\sum_i^N \tau_i}, \quad (1)$$

where τ_i is the transit time for a given sample i and N is the total number of samples. Similar equations were used to calculate the mean y component (\bar{v}) and z component (\bar{w}) of velocity. The Reynolds-stress components were calculated as:

$$\overline{u'v'} = \frac{\sum_i^N (u_i - \bar{u})(v_i - \bar{v})\tau_i}{\sum_i^N \tau_i}, \quad (2)$$

with similar relations for the other five independent components: $\overline{u'u'}$, $\overline{v'v'}$, $\overline{w'w'}$, $\overline{u'w'}$, and $\overline{v'w'}$. Finally, the triple products of the velocity components were calculated as:

$$\overline{u'v'w'} = \frac{\sum_i^N (u_i - \bar{u})(v_i - \bar{v})(w_i - \bar{w})\tau_i}{\sum_i^N \tau_i}, \quad (3)$$

with similar relations for the other nine independent components: $\overline{u'u'u'}$, $\overline{v'v'v'}$, $\overline{w'w'w'}$, $\overline{u'u'v'}$, $\overline{u'u'w'}$, $\overline{u'v'v'}$, $\overline{u'w'w'}$, $\overline{v'v'w'}$, and $\overline{w'w'v'}$. In Eqs. 2 and 3, it is assumed that the u , v , and w velocities are available at the same instant in time and that was ensured by processing only coincident data.

At each measurement location in a flow-field survey, 30,000 samples were typically collected. For the data rates that were achieved with our LDV system (100 to 500 samples/sec), many of the samples were statistically independent, being separated in time by at least two times the integral time scale. In general, the number of samples collected was more than sufficient to achieve well-converged statistical moments.

The processing steps described above apply to the single-channel mode, where the LDV probe is operated with the five green laser beams and a single photomultiplier channel. However, when the probe is operated in the dual channel mode, where both the green and blue lasers are utilized, additional processing steps are required. For brevity, a summary of those steps is provided here, and further details can be found in Kegerise and Neuhart.¹⁸

As noted earlier, the blue laser beams form a converging set of fringes that overlap the measurement volumes formed by the green laser beams. Using the Doppler frequency measured with the converging fringe pattern and the velocity measured with the conventional green-beam measurement volumes, the local fringe spacing in the blue-beam measurement volume was calculated. Then, using a simple linear model for the converging fringe pattern¹⁴ and the calculated local fringe spacing, the position of the particle along the bisector of the measurement volume was calculated. When performing these calculations, only coincident data between the blue and green channels was considered. For the present study, dual-channel measurements were made with the LDV probe oriented normal to the fuselage window surface. That means the measurement volume bisector was normal to the window surface and so particle positions within the measurement volume were measured along that direction. By making a series of closely-spaced measurements in the y direction, where each successive measurement volume overlapped the previous one, a composite point cloud of particle position versus velocity was formed. The particle positions, and the associated velocity components, were then divided into bins along the y direction, each with a width of 40 μm , and statistical moments for the samples in each bin were calculated using Eqs. 1–3. This approach allowed for finer spatial resolution in the near-wall region of the fuselage boundary layer relative to that achieved in the single-channel mode. While a smaller bin width could conceivably be used, the selected value was chosen so that sufficient samples were contained in each bin (approximately 5,000 to 10,000 samples) to ensure well-converged statistics with reasonable measurement uncertainty.

D. Infrared Imaging

Infrared (IR) imaging was used to determine the location of boundary-layer transition on the junction model. This method is based on the detection of surface temperature differences brought about by the increased heat-transfer rates

that occur as the boundary layer transitions from laminar to turbulent flow. Although these surface temperature changes are small in low-speed flows, the current generation of IR cameras can resolve temperature differences on the order of tens of milliKelvins, which is sufficient to reveal the transition location for our test conditions.

For the present experiment, three IR cameras were used. One IR camera was mounted behind a hole in the north wall of the test section to view the port side of the model fuselage. The other two IR cameras were mounted behind holes in the test-section ceiling to view the upper surfaces of the port- and starboard-wing planforms. Once IR imaging of the upper wing surfaces was completed, the two IR cameras were moved and mounted behind holes in the test-section floor to view the lower surfaces of the port- and starboard-wing planforms.

All three IR cameras had cooled Indium Antimonide (InSb) detectors that provide temperature measurements in the mid-wavelength infrared (MWIR) range of 3 to 5 μm . The resolution of the detectors was 1460 x 852 pixels with a pitch of 14 μm , and the noise equivalent temperature difference (NETD) of the detectors was less than 25 mK. Each camera was calibrated for a temperature range from -20 to 350 $^{\circ}\text{C}$ with an accuracy of $\pm 2 ^{\circ}\text{C}$ or 2% of reading. All cameras were fitted with 25 mm, $f/4.0$ lenses for a wide field of view, and each camera was connected to a host PC via a GigE Vision interface for camera control and image acquisition. Adjustments to the overall exposure and contrast of the acquired IR images were made during post processing.

E. Oil-Flow Visualization

Oil-flow visualizations were performed at selected locations on the port side of the junction model for a range of model pitch angles. In the trailing-edge region of the wing-fuselage junction, the oil-flow visualizations allowed us to observe the surface topology of the corner-flow separation and its progression with model pitch angle. Although these visualizations are generally regarded as qualitative in nature, here they were used to obtain approximate measurements of the length and width of the corner-flow separation. That information was then used to guide the selection of an (x, y) -grid of locations for z -direction profile measurements with the LDV system. In the leading-edge region of the wing-fuselage junction, the surface topology revealed by the oil-flow visualizations was used to guide the selection of (x, z) -locations for y -direction profile measurements with the LDV system. In both regions, the oil-flow visualizations provided useful context for the interpretation of velocity and unsteady-pressure measurements.

The oil-flow material was a mixture of 1 part titanium dioxide (TiO_2), 2 parts kerosene, and 0.3 parts oleic acid. The TiO_2 , which serves as a pigment for the mixture, was white and contrasted well against the black painted model surface. The kerosene, which serves as a carrier liquid for the pigment, facilitated the flow visualization by moving under the influence of the local surface shear stress and then evaporated to leave a mean-flow pattern of pigment on the surface. The oleic acid, which serves as a dispersant, kept the TiO_2 from clumping.

Prior to a given run, the oil-flow material was applied to the model surface with foam paint brushes. The tunnel was then ramped up to the desired chord Reynolds number and a live video feed was used to determine when the oil-flow material stopped flowing. After the run, post-test imagery of the oil-flow visualization was acquired. Close-up images of the corner-flow separation at the wing trailing edge, the wing-leading edge region, and any other flow features of interest from a given run were acquired with a 12 megapixel digital SLR camera. Video recordings of the oil-flow development during a run were also saved. Approximate measurements of key flow features in the oil-flow visualizations were made with a ruler with 1 mm divisions.

F. Steady- and Unsteady-Pressure Measurements

The junction model was instrumented with 266 static pressure ports on the F6 wings and 247 static pressure ports on the fuselage. The inner diameter of each pressure port was 597–648 μm (0.0235–0.0255 inch). The locations of these static pressure ports are plotted on a CAD rendering of the junction model in Fig. 11. Electronically scanned pressure (ESP) modules, which were stowed inside the junction model, were used to measure the mean pressure at each port. The full scale range of the modules was 6.89 kPa (1 psid) or 34.47 kPa (5 psid) depending on the expected pressure range of the ports connected to the module, and the modules were referenced to the ambient pressure in the control room of the wind-tunnel facility. Additional mean pressure measurements were made at static pressure ports on the ceiling, the north wall and the south wall of the test section and on a pressure rail mounted to the floor of the first diffuser, just downstream of the test section. The mean total pressures from a set of boundary-layer rakes mounted to the ceiling, the north wall, and the south wall were also acquired. Analysis of the steady pressures is still ongoing and as such, these results will not be presented in this paper.

Unsteady pressure measurements were performed to gain insight to the dynamic nature of the surface pressure field in specific regions of the junction model. Twenty three MEMS piezoresistive pressure transducers were embedded in the starboard wing of the model at the locations plotted on a CAD rendering of the junction model in Fig. 11. Here,

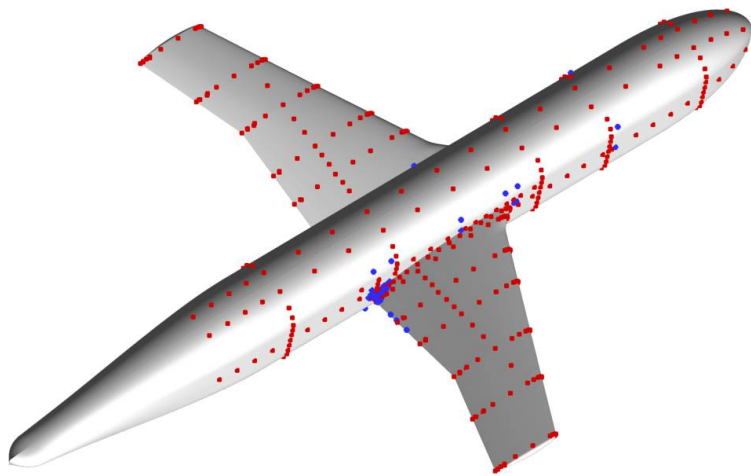


Figure 11. Static pressure port (red squares) and unsteady pressure transducer (blue circles) locations on the junction model configured with the F6 wing with leading-edge extension.

we see that they were clustered near the wing trailing edge, in the corner-flow region. These differential pressure transducers had a full-scale range of 34.5 kPa (5 psid) and a nominal static sensitivity of 72.5 mV/kPa (550 mV/psid). Each of the sensors were referenced to the ambient pressure in the room below the wind tunnel test section. The active element of each sensor was covered by a screen with a 1 mm diameter hole in the center and the screen was set flush to the outer surface of the wing. The frequency response of the sensors was nominally flat from DC to approximately 20 kHz as reported in Hurst *et al.*²⁰ The acceleration sensitivity of the transducers was 5.2×10^{-4} kPa/g equivalent; which for the acceleration levels measured during the test, produces equivalent pressures that are below the noise floor of the measurement system.

An additional thirty one MEMS pressure transducers were embedded in the fuselage of the model at the locations plotted on the CAD rendering of the junction model in Fig. 11. Most of these sensors were located on the starboard side of the fuselage, but a select few were placed on the port side at mirrored locations to examine the symmetry in the unsteady pressure field. The full-scale range, static sensitivity, reference pressure, and acceleration sensitivity of the fuselage sensors were the same as for the wing sensors. In contrast, the active element of each fuselage sensor was not covered by a screen and it was flush mounted with the outer surface of the fuselage. For this configuration, Hurst *et al.*²⁰ have shown that the frequency response for the sensors is extended to approximately 50 kHz. The spatial resolution for each fuselage pressure sensor was 0.5 mm by 0.5 mm.

The voltage signals from the pressure transducers were AC coupled at 0.25 Hz, preamplified, and then passed through an 8th-order low pass filter with a cutoff frequency of 40 kHz for antialiasing. The signals were then digitized with a 24-bit A-to-D converter at a sample rate of 100 kHz. Each channel was sampled simultaneously for a duration of 20 seconds, yielding a total of 2 million samples per channel.

All of the pressure transducers were calibrated *in situ* by applying a range of known pressures to the reference line of each sensor and recording the output voltage through the data acquisition system. A linear regression was then applied to each sensor calibration data set and the static sensitivity was set equal to the slope of the curve fit.

III. Results

In this section, we present sample results for the various measurement techniques that were employed during the test entry. First we present infrared images of the junction model and discuss the natural transition patterns that they revealed. We also present infrared images of the junction model with trip dots applied to fix the transition location. Next we present oil-flow images of the trailing-edge corner-flow separation. This is followed by a presentation of LDV profile measurements on the fuselage nose section, in the leading-edge region of the wing, and in the trailing-edge corner region of the wing. The section finishes with sample results from the unsteady-pressure measurements.

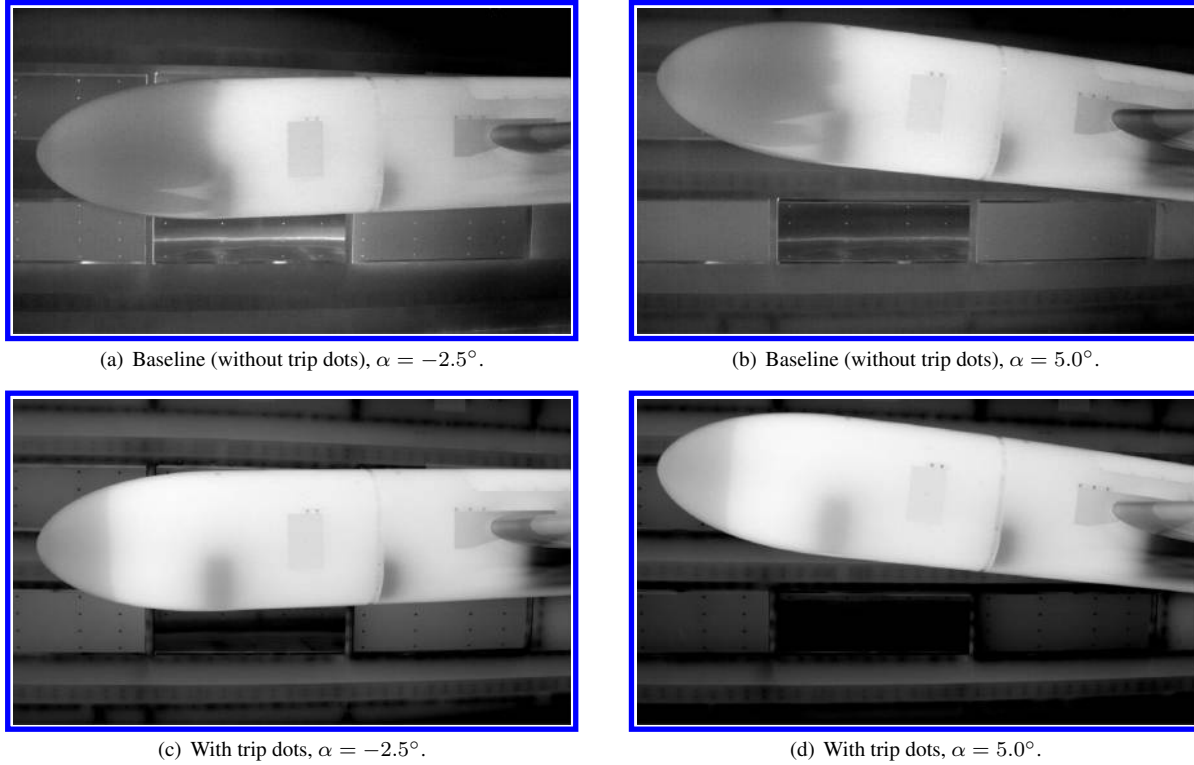


Figure 12. Infrared images of the fuselage port side with and without boundary layer trip dots. F6 wing geometry at $Re_c = 2.4 \times 10^6$.

A. Infrared Imaging Results

The model was initially configured with the F6 wings without the leading-edge extension, and infrared imaging was used to determine the location of natural transition on the fuselage and the upper and lower surfaces of the wings at pitch angles ranging from -10° to 10° . Infrared images of the clean fuselage (no boundary layer trip dots) at model pitch angles of $\alpha = -2.5^\circ$ and 5.0° are shown in Figs. 12a and b. In the images, dark tones correspond to lower (cooler) temperatures and lighter tones correspond to higher (warmer) temperatures. Since the model was cooler than the air temperature, the initially laminar boundary layer on the fuselage nose is marked by dark tones. Boundary-layer transition on the fuselage is then marked by the sudden shift towards lighter tones, where the increased heat transfer associated with the turbulent flow increases the fuselage temperature. It can be seen that the natural transition pattern is somewhat irregular and that the transition location changes slightly with model pitch angle. There are also wedges of turbulent flow ahead of the natural transition location that were found to emanate from small protuberances of paint on the lower side of the fuselage nose.

To ensure a consistent transition location for the fuselage boundary layer, trip dots were placed on the model at a nominal location of $x = 336$ mm from the fuselage nose apex. This location was chosen so that: 1) the trip dots were nominally positioned just downstream of the suction peak as determined from computed pressure distributions at our test conditions and 2) the local Reynolds number based on distance along the surface, Re_s , was greater than 100,000 to ensure fully effective trip dots.²¹ The height of the trip dots was based on the roughness correlations of Braslow and Knox,²² and for our test conditions, the trip dots had a height of $289.4 \pm 1.1 \mu\text{m}$ (0.0114 in). The trip dots were cylindrical in shape with a diameter of 1.16 ± 0.03 mm and had a center-to-center spacing of 2.47 ± 0.04 mm. Infrared images for the tripped fuselage at model pitch angles of $\alpha = -2.5^\circ$ and 5.0° are shown in Figs. 12c and d. Here, it is observed that the transition location is fixed at the trip dots and does not vary with model pitch angle.

Infrared images of the clean starboard and port F6 wings at model pitch angles of $\alpha = -2.5^\circ$ and 5.0° are shown in Figs. 13a–b and 14a–b. Except for a few wedges of turbulent flow induced by imperfections in the painted surface, the overall transition pattern between the starboard and port wings is similar at each pitch angle considered. The darker tones near and along the length of the wing leading edges indicates that laminar flow prevails in this region. Although the fuselage boundary layer is turbulent near the wing root, it does not contaminate the wing leading edge because the attachment-line Reynolds number is too low to sustain turbulent flow. For pitch angles above $\alpha = -2.5^\circ$, the transition location was found to rapidly advance forward along the entire wing span, and by $\alpha = 2.5^\circ$, the transition

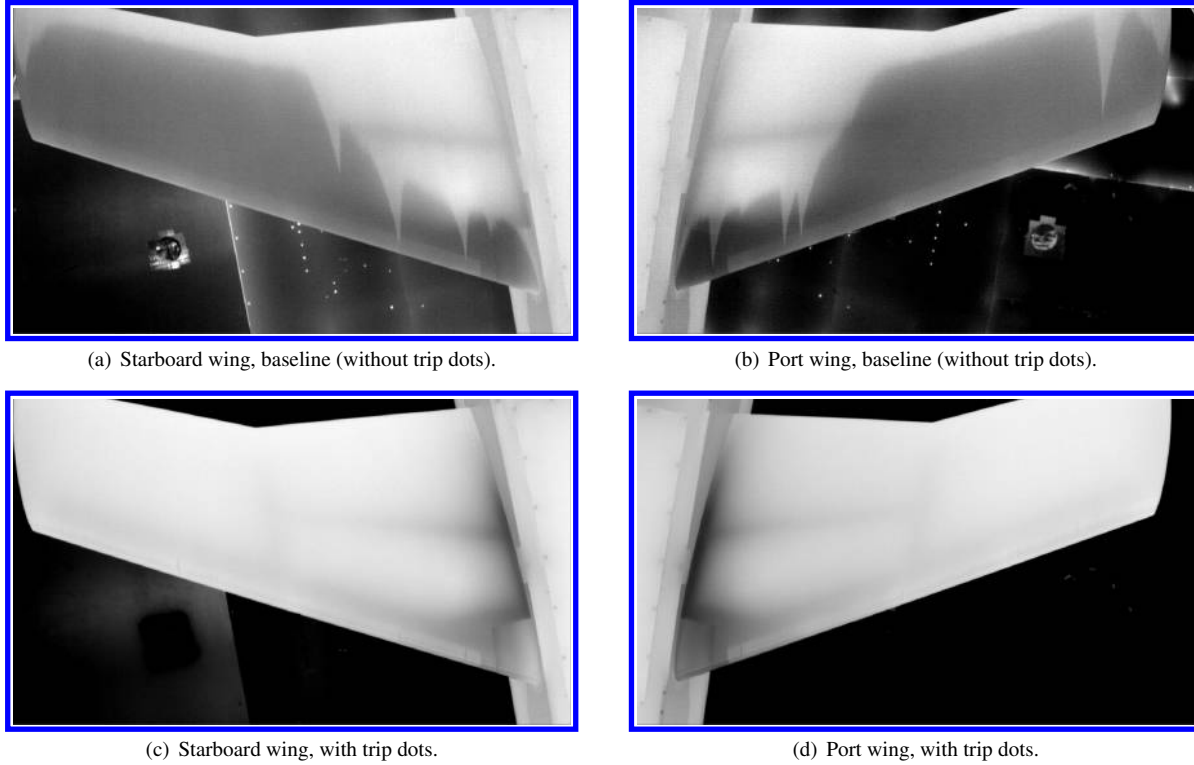


Figure 13. Infrared images of the upper wing surfaces, with and without boundary layer trip dots, at $\alpha = -2.5^\circ$. F6 wing geometry at $Re_c = 2.4 \times 10^6$.

location locked into a distance from the wing leading edge that was nearly fixed with further increases in the pitch angle. This behavior suggests that a leading-edge separation bubble forms and reattaches turbulent.

To eliminate the leading-edge separation bubble, trip dots with a height of $170.6 \pm 2.5 \mu\text{m}$ (0.0067 in) were placed just upstream of the separation bubble along a line positioned at an arc-distance from the leading-edge equal to 1.6% of the local chord. These trip dots were also cylindrical in shape with a diameter of $1.27 \pm 0.02 \text{ mm}$ and had a center-to-center spacing of $2.53 \pm 0.04 \text{ mm}$. The resulting IR images of the upper wing surfaces at model pitch angles of $\alpha = -2.5^\circ$ and 5.0° are shown in Figs. 13c-d and 14c-d, and here, boundary-layer transition was fixed at the trip-dot location.

Trip dots were also applied to the lower wing surfaces to fix the transition location. These trips dots were placed along a line at an arc distance from the leading edge equal to 10% of the local chord and were cylindrical in shape with a height of $196.9 \pm 1.3 \mu\text{m}$ (0.0078 in), a diameter of $1.24 \pm 0.03 \text{ mm}$, and a center-to-center spacing of $2.42 \pm 0.09 \text{ mm}$. With these trip dots, boundary-layer transition was fixed at the trip-dot location for model pitch angles of -5° and above.

Infrared imaging for the F6 wing with the leading-edge extension was not performed during our test entry. However, when switching from the F6 wing to the F6 wing with extension, the only model parts that changed were the removable inserts around the leading-edge root region. The trip dots on the remainder of the model were undisturbed and a new set of trip dots were placed on the leading-edge extensions of the port and starboard wings. With the leading-edge extension, the fuselage boundary layer does contaminate the insert attachment line, but outboard of the the insert, the flow relaminarizes since the attachment line Reynolds number is too low to sustain a turbulent boundary layer.⁷ Other than that difference, the tripped transition locations on the fuselage and the upper and lower wing surfaces were expected to remain the same for this configuration.

B. Oil Flow Visualization Results

Oil-flow visualizations in the trailing-edge corner region of the F6 wing with leading-edge extension are shown in Fig. 15 for a range of model pitch angles. Here we observe the occurrence of separated flow and a progressive growth in the separated-flow region with increasing pitch angle. Measurements of the corner-flow separation length, ℓ , and width, w , were made with a ruler with 1 mm divisions. Generally, the corner-flow separation is marked by a diffuse

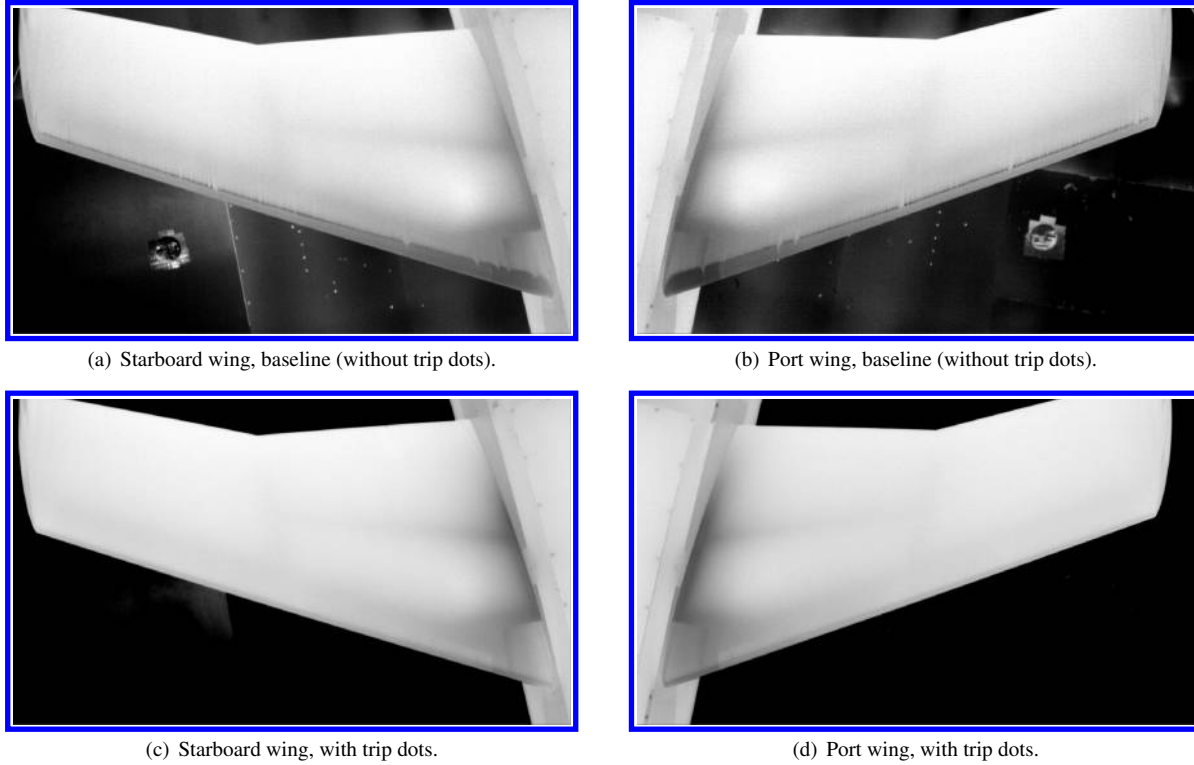


Figure 14. Infrared images of the upper wing surfaces, with and without boundary layer trip dots, at $\alpha = 5.0^\circ$. F6 wing geometry at $Re_c = 2.4 \times 10^6$.

band of oil-flow material at the boundary of the separation. This is due to the unsteady nature of the corner-flow separation and the history of the oil-flow development as a run proceeds. As such, it is difficult to say precisely where the mean separation line is located. For the present study, we report the outer extent (length and width) of this band of oil-flow material, and an example length and width measurement is annotated in Fig. 15c. With this definition, it is likely that the true length and width bounding the mean separation line is less than what is reported here. While this is acceptable for identifying trends and in helping to guide the selection of survey regions for the LDV measurements, it should be used with caution—keeping in mind the limitations—when comparing to CFD calculations. Table 1 lists the separation lengths and widths on the F6 wing with leading-edge extension for the pitch angles considered. Uncertainty estimates are also included in the table and they denote the 95% confidence level. Note that the oil-flow visualizations were performed only on the port side of the model since the unsteady pressure sensors on the starboard side precluded the use of oil flow.

Table 1. Measured widths and lengths (with uncertainties) of the corner-flow separation for the F6 wing with leading-edge extension (port side).

α ($^\circ$)	w (mm)	U_w (mm)	ℓ (mm)	U_ℓ (mm)
-2.5	22.0	3.6	81.0	10.7
0	29.5	4.7	89.0	11.7
2.5	38.0	6.1	104.0	13.7
5	42.5	6.8	118.5	15.5
10	54.0	8.7	152.0	19.9

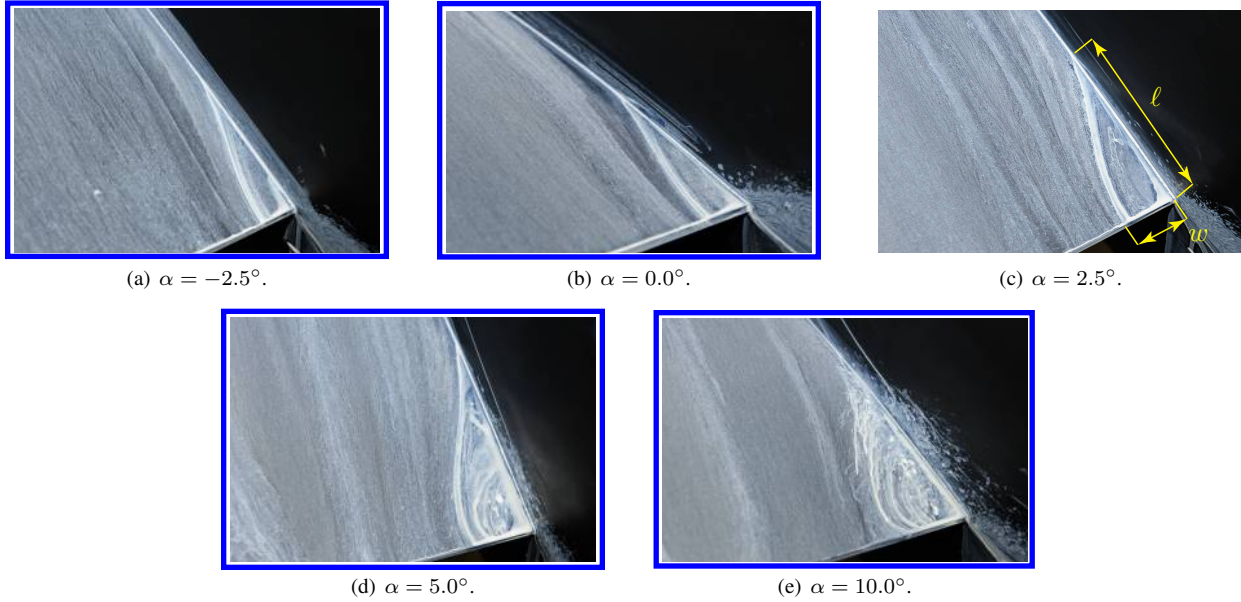


Figure 15. Oil-flow visualizations in the trailing-edge corner of the F6 wing with leading-edge extension (port side) versus model pitch angle.

C. LDV Measurement Results

Over the course of the test entry, LDV profile measurements were made for three cases: the F6 wing at a model pitch angle of 5° , the F6 wing with leading-edge extension at a model pitch angle of -2.5° , and the F6 wing with leading-edge extension at a model pitch angle of 5° . For each case, velocity profiles were measured on the fuselage nose section, in the leading-edge region of the wing, and in the trailing-edge corner region of wing. All of the LDV measurements were made on the port side of the junction model and the planform break chord Reynolds number was held constant at 2.4×10^6 . In this section, sample results will be presented for the F6 wing with leading-edge extension at a model pitch angle of 5° . Sample results for the other test cases can be found in Kegerise and Neuhart.¹⁸

1. LDV Measurements on the Fuselage Nose Section

With the LDV probe/traverse system positioned in the fuselage nose section, velocity profiles were acquired by traversing in the $-y$ direction, normal to the port side of the fuselage. The intent here was to provide measurements of the fuselage boundary layer, well upstream of the wing leading edge, where the flow is attached and RANS turbulence models are expected to perform well. Profile measurements were made at $x = 1168.4$ mm and $z = 0$ mm, ± 30 mm, and ± 60 mm. Repeat profile measurements were also made at a subset of those locations to assess the run-to-run repeatability. Each profile typically contained 30 y locations, with a logarithmic spacing between locations, and the first location from the window surface was typically $200 \mu\text{m}$. To put that into perspective, one wall unit ($y^+ = yu_\tau/\nu = 1$) was approximately $6.5 \mu\text{m}$ for our test conditions and so for the first location off the surface, the center of the measurement volume was at roughly $y^+ \approx 31$. However, the LDV probe was operated in the dual-channel mode for these measurements and the resulting particle positions within the measurement volume were used to improve the near-wall spatial resolution via the binning method described in the Experimental Methods section. With that, velocity statistics were calculated for a location as close as $150 \mu\text{m}$ ($y^+ \approx 23$) from the fuselage surface.

Mean-velocity and Reynolds-stress profiles at $x = 1168.4$ mm, $z = 0$ mm, on both linear and semilogarithmic scales, are shown in Fig. 16. Here, three repeat profile measurements, acquired over a period of days to weeks, are presented. Uncertainty bands are included in each profile plot and they represent the uncertainty for a 95% confidence level. The mean-velocity components were normalized by the freestream velocity and the Reynolds-stress components were normalized by the freestream velocity squared (this was done throughout all of the LDV profile plots presented in this paper). The y locations for the profiles are referenced to the fuselage surface at $y_o = -236.1$ mm.

The \bar{u} component of mean velocity is similar to that of a zero-pressure-gradient (ZPG) turbulent boundary layer, with a distinct log region and a wake region. The \bar{v} component of mean velocity is essentially zero across the boundary layer and the \bar{w} component of mean velocity is positive, which reflects the fact that the model is pitched upward. The

Reynolds normal stress profiles are also similar in shape to those of a ZPG turbulent boundary layer and have similar anisotropy, with the $\bar{u}'\bar{u}'$ component being the largest, followed by the $\bar{w}'\bar{w}'$ component and then the $\bar{v}'\bar{v}'$ component. The largest amplitude for the $\bar{u}'\bar{u}'$ component occurs at the first measurement location off the surface, where the peak in turbulent production is approached, but not quite reached. For the Reynolds shear stress profiles, the $\bar{u}'\bar{v}'$ component has a distribution similar to that of a ZPG turbulent boundary layer; but in the present case, the values are positive as opposed to the negative values observed in the canonical ZPG case. This is simply a reflection of our coordinate system, which has the y direction, and hence the v component of velocity, positive towards the port side of the fuselage. In contrast to a ZPG turbulent boundary layer, the $\bar{u}'\bar{w}'$ and $\bar{v}'\bar{w}'$ components of Reynolds shear stress are nonzero across the boundary layer due to the spanwise mean flow at this model pitch angle and x location. While the $\bar{u}'\bar{v}'$ component is dominant and nearly constant across the log region of the boundary layer, the $\bar{u}'\bar{w}'$ component is observed to become dominant in the near-wall region. For all of the velocity statistics presented in Fig. 16, the repeat profile measurements were generally within the measurement uncertainty. The mean-velocity and Reynolds-stress profiles at z locations above and below $z = 0$ mm (not shown here) were found to be similar and nearly the same in view of the measurement uncertainty.

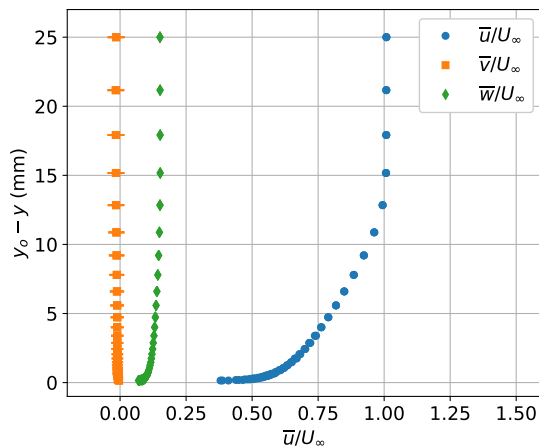
2. LDV Measurements in the Wing Leading Edge Region

With the LDV probe/traverse system positioned near the wing leading edge, velocity profiles were again acquired by traversing in the $-y$ direction, normal to the port side of the fuselage. The LDV probe was operated in the single-channel mode for most of the measurements in this region and each profile contained 25 uniformly spaced y locations starting at 500 μm from the fuselage surface. A schematic of the (x, z) measurement locations is shown in Fig. 17 and it is superimposed on an oil-flow visualization of the leading-edge region. In part, the selected measurement locations were dictated by the optical access afforded by the window insert. For that insert, the thin acrylic window (1 mm thick) was bonded to a frame of supporting ribs that minimized deflection under load, but limited the regions where profile measurements could be made. The oil-flow visualization reveals a stagnation region on the fuselage below the wing chord line (the red dashed line in Fig. 17) and a single separation line emanates from that region. Due to the weaker adverse pressure gradient imposed by the wing leading-edge extension that tapers into the fuselage almost tangentially, the separation line lies fairly close to the wing leading edge, particularly over the upper surface of the wing. This is in contrast to the F6 wing *without* the leading-edge extension where a strong horseshoe vortex is present and multiple separation lines are observed ahead of the wing leading edge.¹⁸

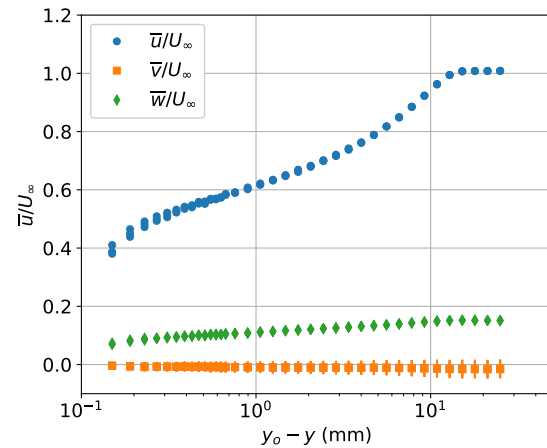
Mean-velocity profiles at four x locations along a line at $z = 98.05$ mm are shown in Fig. 18. As before, uncertainty bands are included for each profile plot and the y locations for the profiles are referenced to the fuselage surface at $y_o = -236.1$ mm. For the chosen x locations, the fuselage boundary layer is still attached and the \bar{u} profiles do not change significantly as the leading edge is approached. The \bar{v} profiles are essentially zero across the boundary layer while the \bar{w} profiles are positive, reflecting the fact that the model is at a positive pitch angle. In addition, the \bar{w} shifts to larger values with increasing x location and the total mean-flow profile becomes more skewed as the oncoming flow is directed up and around the leading edge. The Reynolds normal-stress profiles at the same four locations along the line at $z = 98.05$ mm are shown in Fig. 19. Here, the $\bar{v}'\bar{v}'$ and $\bar{w}'\bar{w}'$ components do not vary significantly as the leading-edge is approached; however, the $\bar{u}'\bar{u}'$ component does display some near-wall attenuation and the development of a peak away from the surface with increasing x location. The corresponding Reynolds shear-stress profiles are shown in Fig. 20 and they are similar for the four locations considered. The $\bar{u}'\bar{v}'$ component is observed to peak away from the wall, near $y_o - y = 5$ mm, and both the $\bar{u}'\bar{w}'$ and $\bar{v}'\bar{w}'$ components are increasingly positive moving toward the wall. The edge of the boundary layer in this region of the fuselage is at roughly 25 mm and the Reynolds stresses approach the freestream values above that height. Additional profile measurements in the leading-edge region of the wing can be found in Kegerise and Neuhart.¹⁸

3. LDV Measurements in the Wing Trailing Edge Region

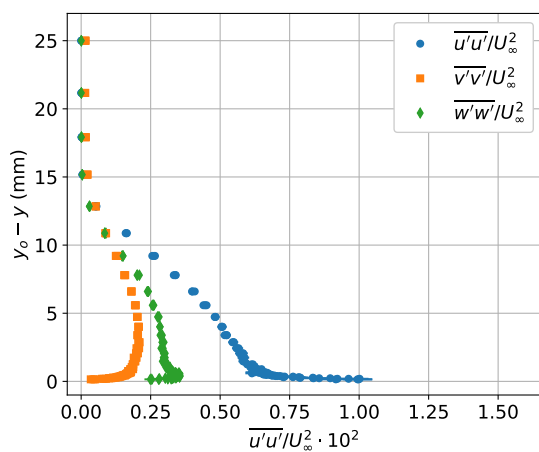
With the LDV probe/traverse system positioned near the wing trailing edge, velocity profiles were acquired by traversing in the z direction, up from the wing surface, for a range of (x, y) locations. The LDV probe was operated in the single-channel mode for these measurements and the probe optical axis was tilted downward by 10° in the (y, z) plane so that the measurement volume could be placed closer to the wing surface without clipping some of the probe beams. Each profile contained 30 z locations starting at 500 μm from the wing surface. A z location closer to the wing surface could not be achieved due to laser flare noise. The (x, y) locations at which profile measurements were made are plotted in Fig. 21 and they are overlaid on an oil-flow visualization for a spatial reference. Profile measurements were



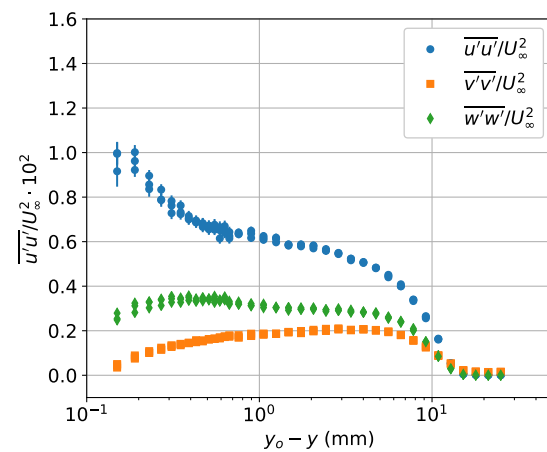
(a) Mean velocities.



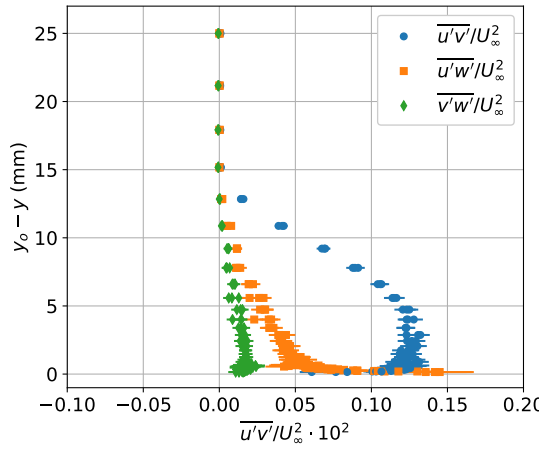
(b) Mean velocities



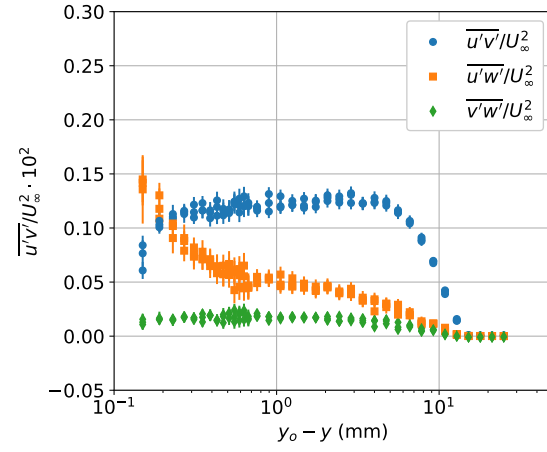
(c) Reynolds normal stresses.



(d) Reynolds normal stresses.



(e) Reynolds shear stresses.



(f) Reynolds shear stresses.

Figure 16. Mean-velocity and Reynolds-stress profiles (on both linear and semilogarithmic scales) on the fuselage nose section of the junction model at $x = 1168.4$ mm, $z = 0$ mm, and $\alpha = 5^\circ$. Three repeat profile measurements are shown in the plots.

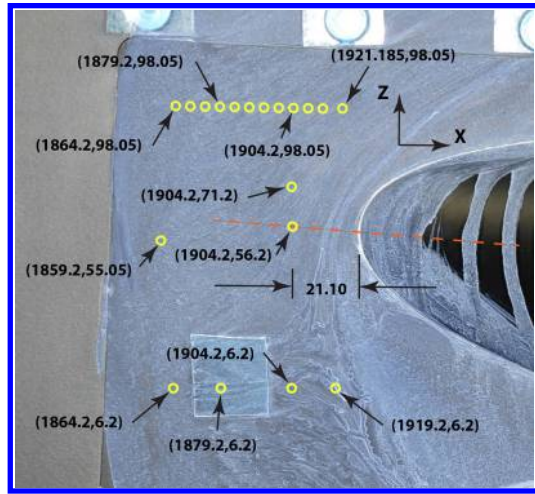


Figure 17. Schematic of the LDV measurement locations in the leading-edge region of the F6 wing with leading-edge extension at a model pitch angle of 5° . The yellow circles denote locations where profile measurements were made and the red dashed line denotes the chord line of the wing root section. Dimensions are in millimeters.

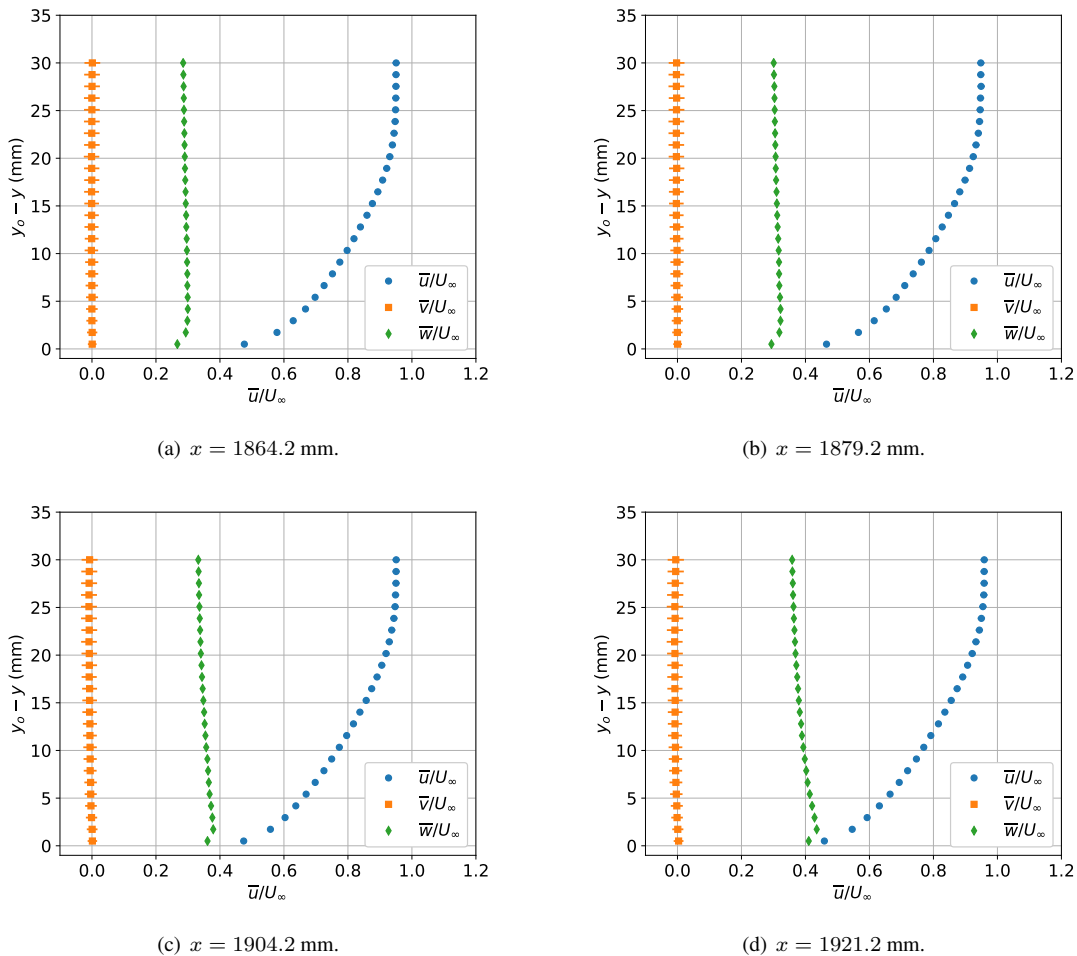


Figure 18. Mean-velocity profiles along a line located at $z = 98.05$ mm near the wing leading edge.

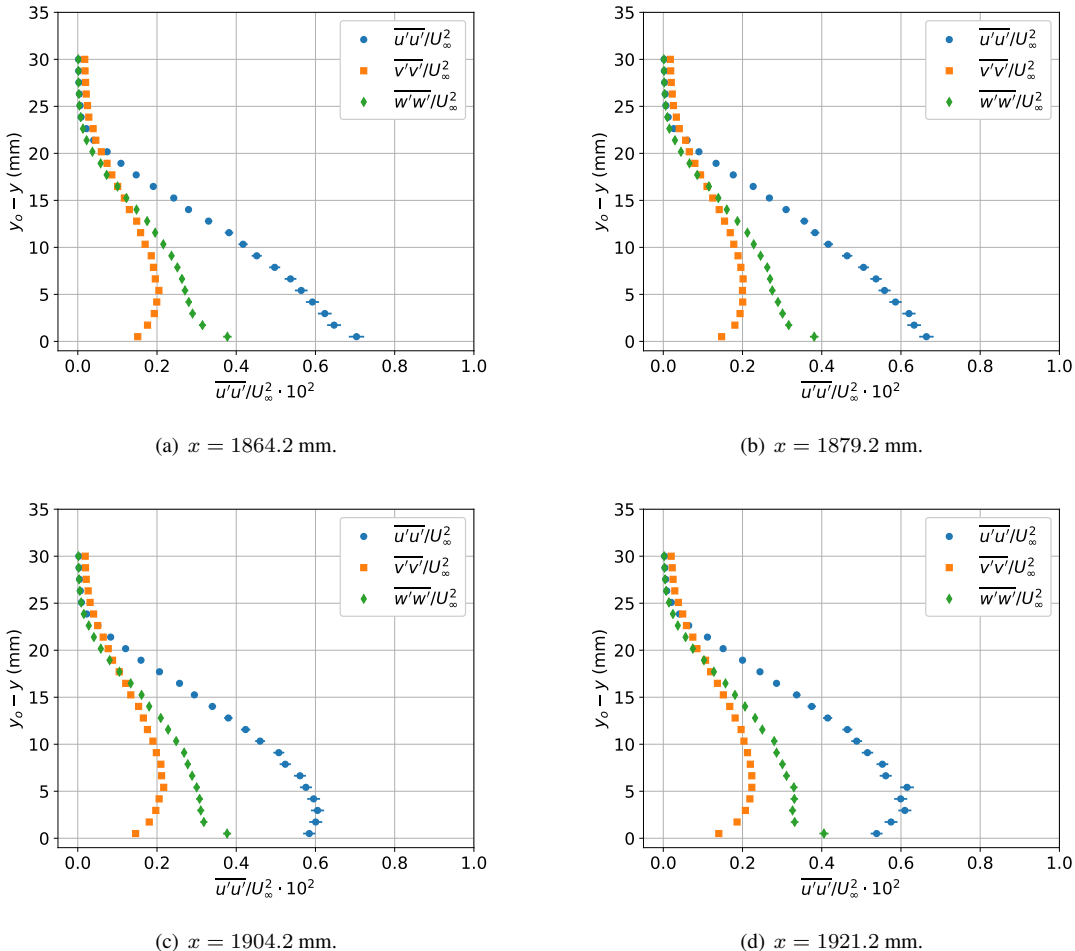


Figure 19. Reynolds normal-stress profiles along a line located at $z = 98.05$ mm near the wing leading edge.

made at 45 unique (x, y) locations and an additional 19 repeat profile measurements, distributed over those locations, were made to assess run-to-run repeatability.

Mean-velocity profiles for six spanwise locations (y locations) at $x = 2852.6$ mm are shown in Fig. 22. This x location is close to the beginning of the separated corner flow as indicated by the oil-flow visualization (see Fig. 21). For reference, the fuselage surface was located at $y = -236.1$ mm and z_o in the ordinate label denotes the z location of the wing surface. At the last spanwise location shown (Fig. 22f), the profiles extend over a smaller range of z values and this is due to support ribs on the optical windows that blocked some of the probe laser beams and thereby prevented measurements. Depending on the y location of a profile, a given $z - z_o$ position may be in the fuselage boundary alone, the wing boundary alone, in the merged area of both, or out in the freestream. For $z - z_o$ locations of approximately 20 mm and above, the variations in the mean-velocity profiles are mainly associated with the fuselage boundary layer. As we move outboard along the wing span to larger $-y$ values, the \bar{u} component increases towards the local freestream value. The \bar{v} component is essentially zero in this region and the \bar{w} component is negative as the flow is moving down along the contour of the wing surface. For $z - z_o$ locations below approximately 20 mm, the variations in the mean-velocity profiles are mainly associated with the merged fuselage and wing boundary layers just as the corner-flow separation begins. In this region, the \bar{u} profiles near the fuselage (Figs. 22a–d) have an inflectional character, but as we move outboard, the \bar{u} profiles become fuller and at the last spanwise location (Fig. 22f), we are outside of the fuselage boundary layer and the profile is indicative of the wing boundary layer. For the two spanwise locations closest to the fuselage surface (Figs. 22a–b), the \bar{u} velocity at $500 \mu\text{m}$ off the wing surface is near zero. However, an inspection of the histogram for the instantaneous values of u (not shown here) reveals a bimodal character indicating periods of time where the flow is either reversed (negative u) or attached (positive u). For spanwise locations near the fuselage surface, the \bar{v} component of velocity is near zero; however, as we move to larger $-y$ locations, the \bar{v} component becomes increasingly negative, indicating spanwise flow away from the fuselage. In part, this is due to the upstream

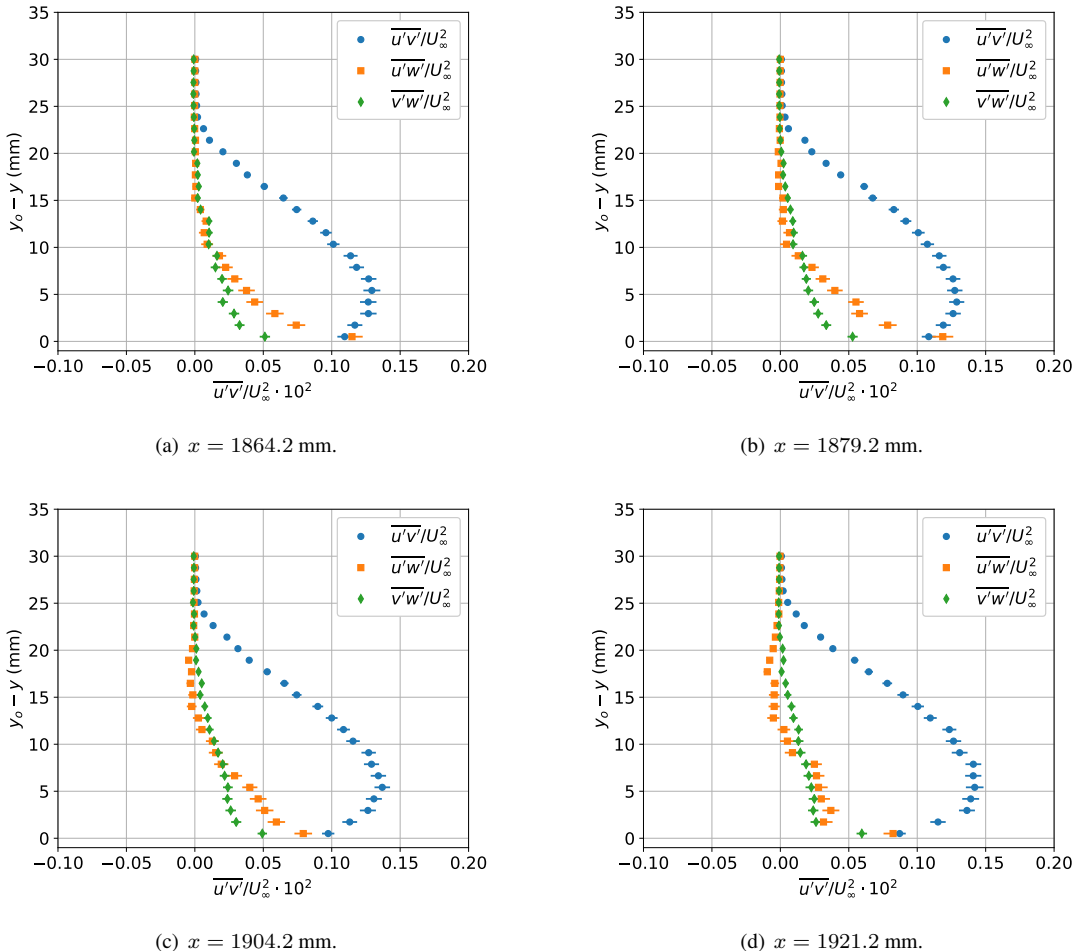


Figure 20. Reynolds shear-stress profiles along a line located at $z = 98.05$ mm near the wing leading edge.

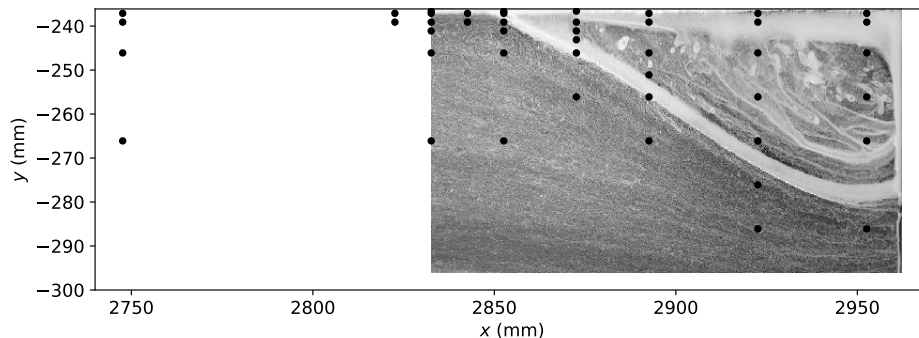


Figure 21. Locations of z -direction LDV surveys in the corner-flow region of the F6 wing with leading-edge extension. The black circles denote the (x, y) -locations of the profiles and those locations are superimposed on an image of the oil-flow visualization at $\alpha = 5^\circ$.

influence of the expanding corner flow separation region.

Reynolds normal-stress profiles for the same six spanwise locations at $x = 2852.6$ mm are shown in Fig. 23. Similar to the mean-velocity profiles, the Reynolds normal-stress variations above a $z - z_o$ of approximately 20 mm are mainly associated with the fuselage boundary layer. Here, all three components of normal stress increase in amplitude as we move outboard along the wing surface and then they decay to the freestream values as we exit the

fuselage boundary layer at $y = -266.1$ mm. Below a $z - z_o$ of approximately 20 mm, the normal-stress variations are mainly driven by the interaction of the merged wing and fuselage boundary layers just as the corner-flow separation begins. By $y = -266.1$ mm, however, the character of the normal-stress profiles has changed and the variations are associated with the wing boundary layer.

The corresponding Reynolds shear-stress profiles at $x = 2852.6$ mm are shown in Fig. 24. Again, the Reynolds shear-stress variations above $z - z_o$ of approximately 20 mm are mainly associated with the fuselage boundary layer. Here, the $\bar{u}'\bar{v}'$ component is the largest and as we move outboard, it increases in magnitude before decaying to the freestream level once we are outside of the fuselage boundary layer. In contrast, the $\bar{u}'\bar{w}'$ and $\bar{v}'\bar{w}'$ components are negative and decrease towards zero as we move outboard and out of the fuselage boundary layer. In the region below $z - z_o$ of approximately 20 mm, there are significant shear-stress variations that are again driven by the interaction of the merged wing and fuselage boundary layers just as the corner-flow separation begins. Outside of the fuselage boundary layer at $y = -266.1$ mm, the variations in the Reynolds shear stresses are indicative of the wing boundary layer.

Mean-velocity profiles for six spanwise locations at $x = 2892.6$ mm are shown in Fig. 25. This x location is 40 mm downstream of the beginning of the corner-flow separation, and some of the profiles were acquired inside the separated-flow region. At the first two y locations away from the fuselage surface ($y = -237.1$ mm and $y = -239.1$ mm), the \bar{u} values are negative near the wall, indicating reversed flow in the mean. Here also, the near-wall \bar{w} values are positive, indicating flow is moving upstream along the contour of the wing surface. An inspection of the histograms for the instantaneous values of both u and w (not shown here) reveals bimodal distributions from the first point off the wall at 500 μm , up to 10 mm away from the wall. This suggests a highly unsteady separated flow region that exhibits periods of attached flow and periods of separated flow. Moving farther outboard, but at locations still inside the separated flow region ($y = -246.1$ mm and $y = -251.1$ mm), there is no longer reversed flow in the mean. Outside the separated flow region ($y = -256.1$ mm and $y = -266.1$ mm), the profiles are beginning to take on the character of the wing boundary layer.

The corresponding Reynolds normal-stress profiles at $x = 2892.6$ mm are shown in Fig. 26. For the profile near the fuselage surface ($y = -236.1$ mm and $y = -239.1$ mm), the normal-stress profiles have the character of a free shear layer with peak values near the inflection point in the \bar{u} profile. As we move farther outboard, the peak in the normal-stress profiles shifts towards the wall as the inflection point in the \bar{u} profile also shifts towards the wall. By $y = -266.1$ mm, we are outside of the separated flow region, near the edge of the fuselage boundary layer, and the normal-stress profiles begin to take on the character of the wing boundary layer. The corresponding Reynolds shear-stress profiles at $x = 2892.6$ mm are shown in Fig. 27. Similar to the normal-stress profiles, the $\bar{u}'\bar{w}'$ component displays a peak near the inflection point in the \bar{u} profile, and that peak shifts towards the wall as we move outboard from the fuselage surface. The $\bar{u}'\bar{v}'$ and $\bar{v}'\bar{w}'$ components of shear stress display rather complex variations in the separated flow region and change rapidly with y location as we move outboard and across the separated flow region. As expected, the shear-stress profiles take on the character of the wing boundary layer outside of the separated flow region and fuselage boundary layer at $y = -266.1$ mm.

To give a sense of the run-to-run measurement repeatability in the separated corner flow, repeat profiles for the mean velocity, Reynolds normal stress and Reynolds shear stress at $x = 2892.6$ mm, $y = -239.1$ mm are presented in Fig. 28. In the plots, each velocity statistic is represented by a different symbol and the different colors for each symbol represent the different repeat profiles. Six repeat profiles were acquired at this location over the course of a month. During that period, the LDV probe/traverse assembly was moved to a new location on the bridge piece inside the model (but one in which the traverse travel was sufficient to reach the same (x, y) location on the model). Since that could slightly alter the angles between the probe laser beams and the window-surface normal, the beam unit vectors were remeasured after moving the assembly and a new velocity transformation matrix was calculated. In general, the scatter in the statistics at a given $z - z_o$ location appears to be random from run-to-run and most of the scatter can be accounted for by the estimated measurement uncertainties (uncertainty bands are not shown in the plots to improve clarity).

As a final example of the LDV measurements, triple-products of the velocity components measured at $x = 2892.6$ mm, $y = -239.1$ mm are shown in Fig. 29. In these plots, the ten independent triple-product components were normalized by U_∞^3 and therefore, the amplitudes are very small. To reduce the number of decimal places on the abscissas of the plots, the normalized triple products were multiplied by 10^3 . Six repeat measurements of the triple products at this location on the model were performed over the course of a month, and most of the points in the repeat profiles were found to be within the measurement uncertainty.

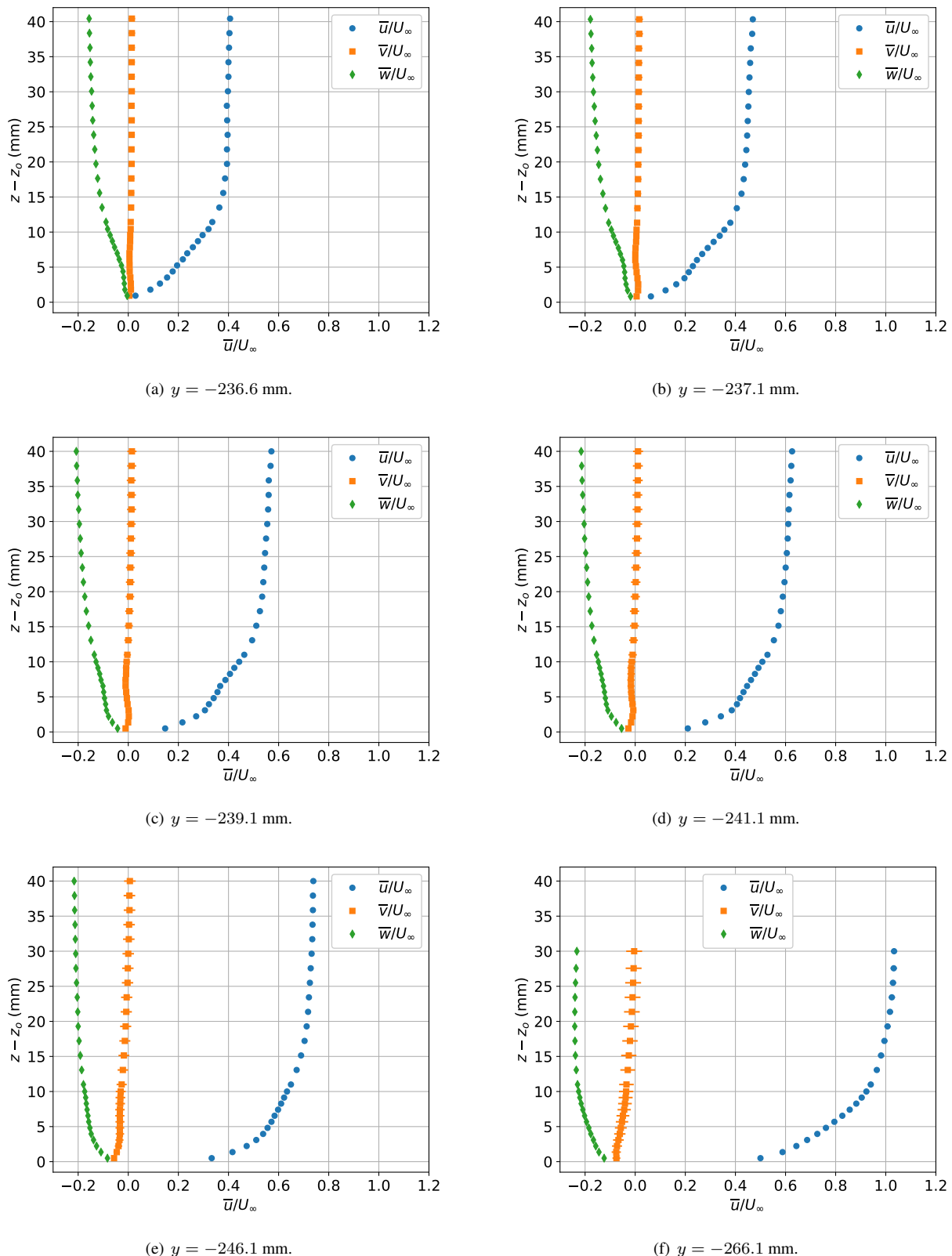


Figure 22. Mean-velocity profiles in the corner-flow region of the F6 wing with leading-edge extension at $x = 2852.6$ mm and $\alpha = 5^\circ$.

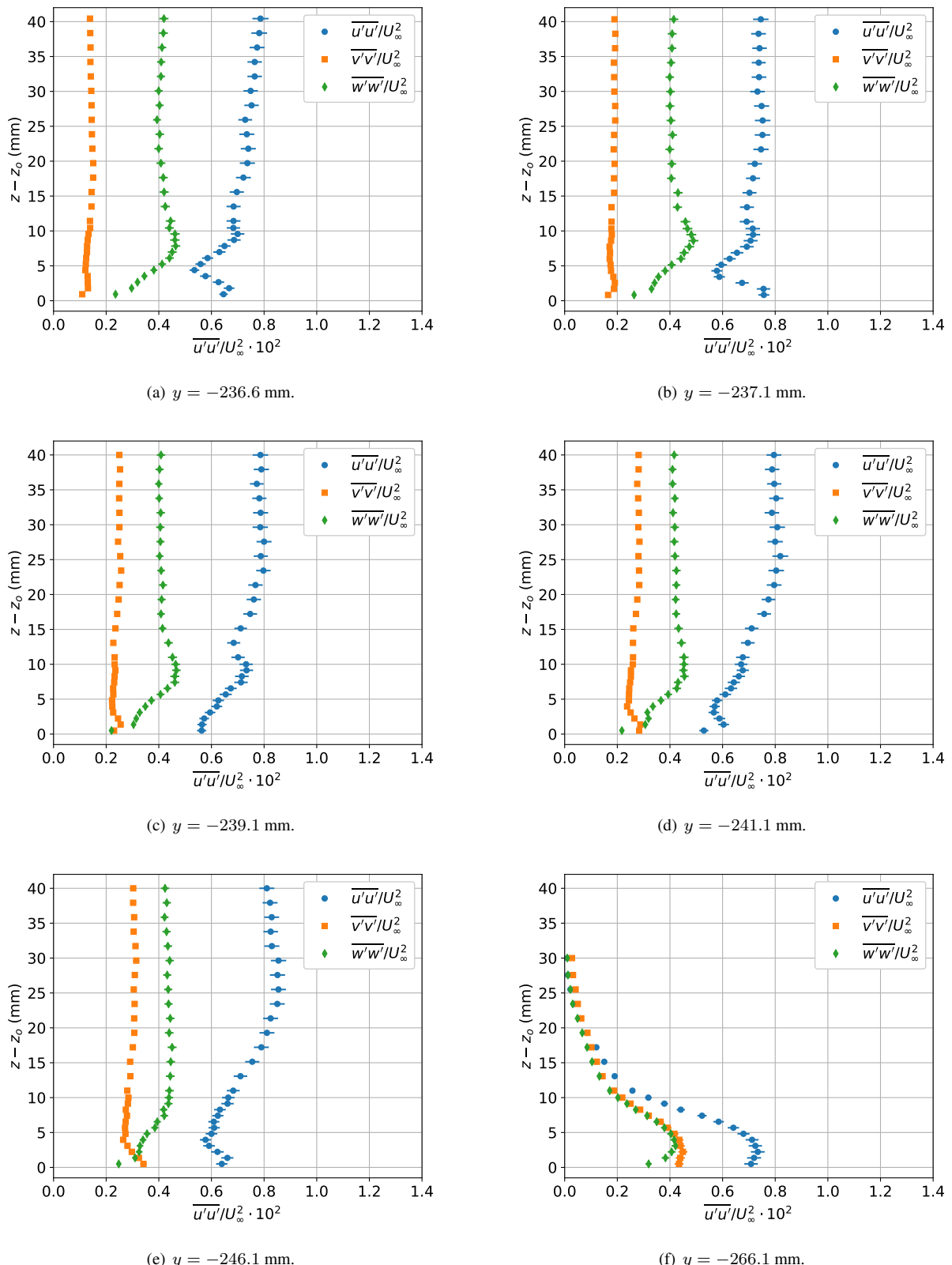


Figure 23. Reynolds normal-stress profiles in the corner-flow region of the F6 wing with leading-edge extension at $x = 2852.6 \text{ mm}$ and $\alpha = 5^\circ$.

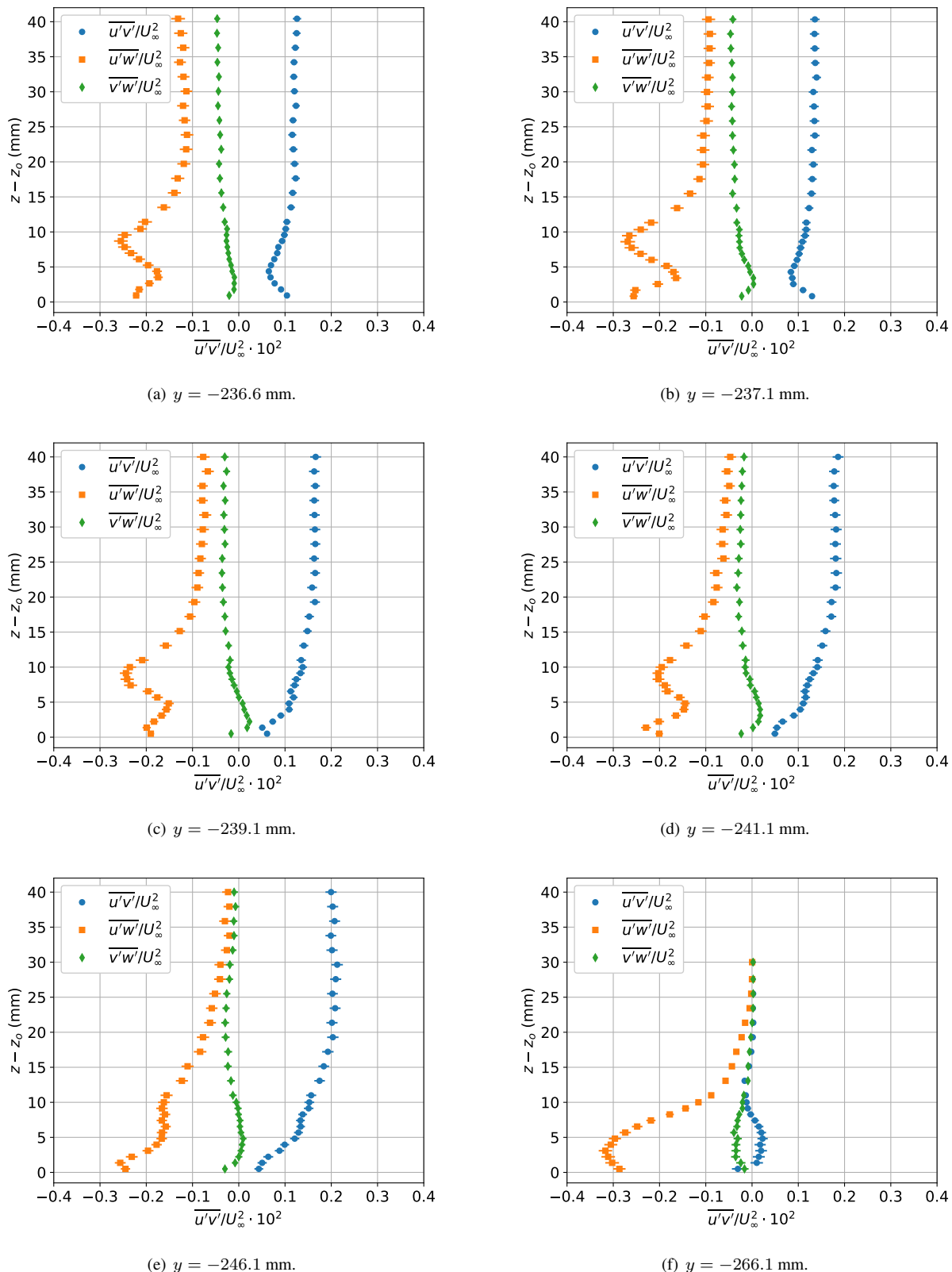


Figure 24. Reynolds shear-stress profiles in the corner-flow region of the F6 wing with leading-edge extension at $x = 2852.6$ mm and $\alpha = 5^\circ$.

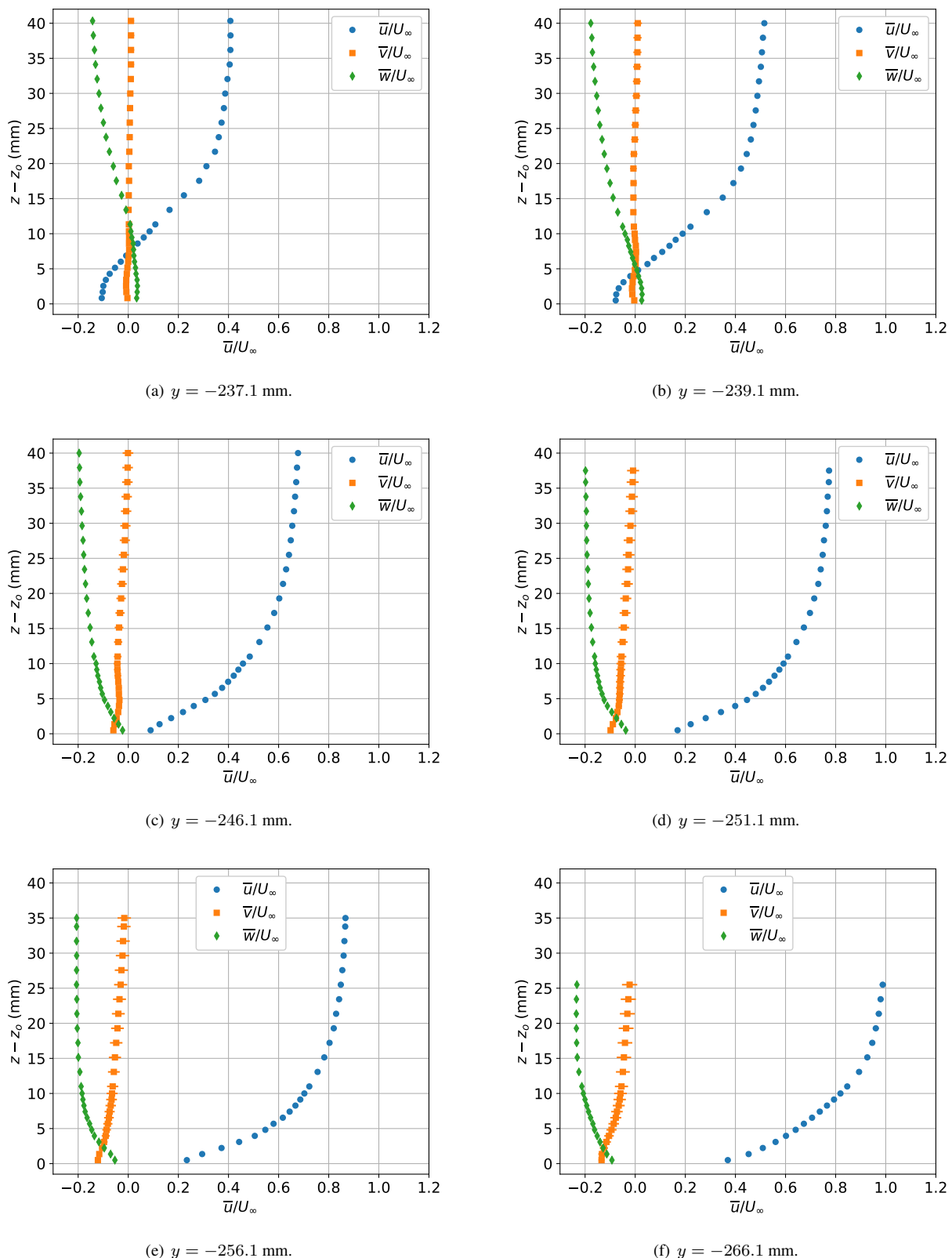


Figure 25. Mean-velocity profiles in the corner-flow region of the F6 wing with leading-edge extension at $x = 2892.6$ mm and $\alpha = 5^\circ$.

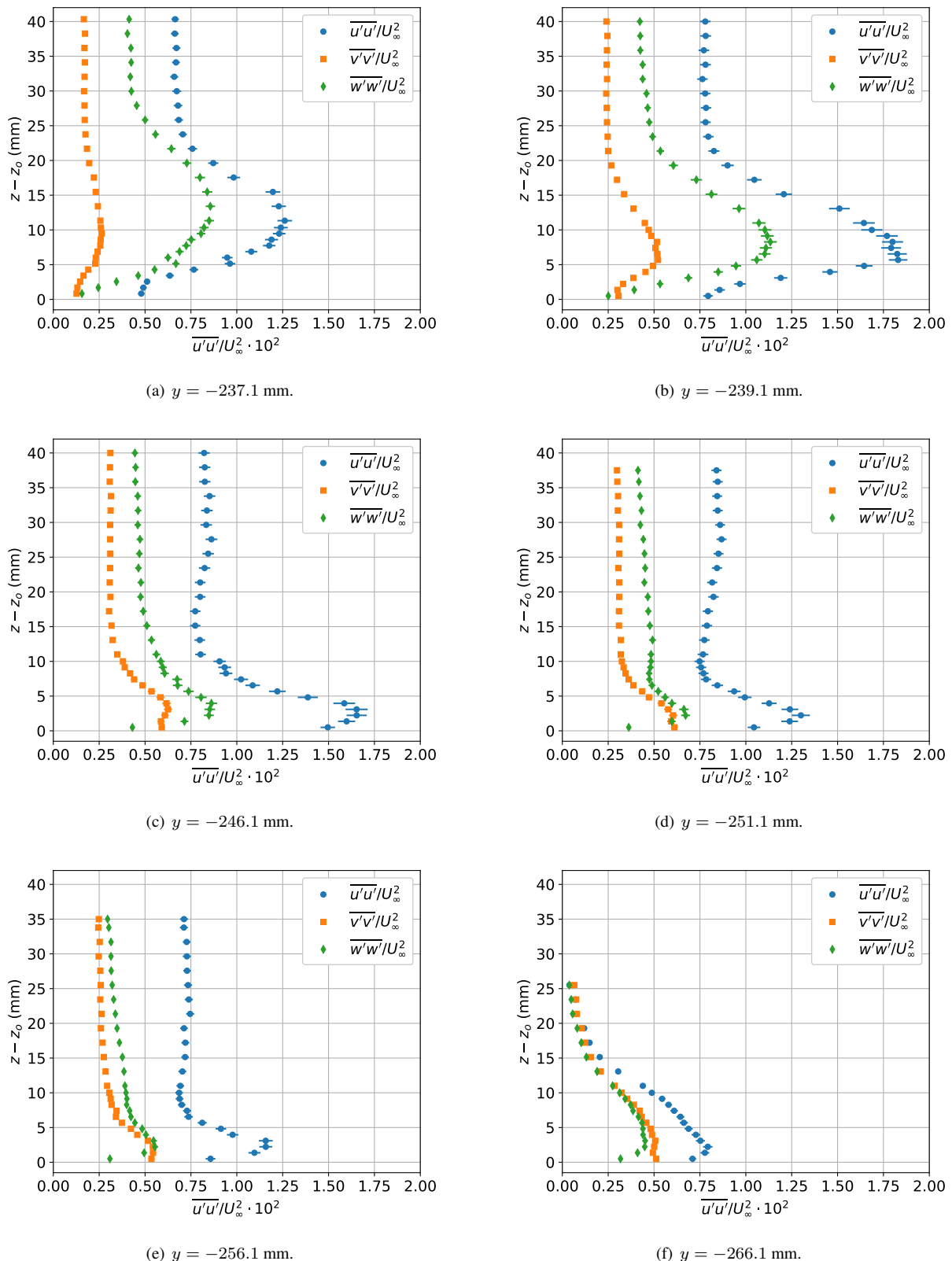


Figure 26. Reynolds normal-stress profiles in the corner-flow region of the F6 wing with leading-edge extension at $x = 2892.6$ mm and $\alpha = 5^\circ$.

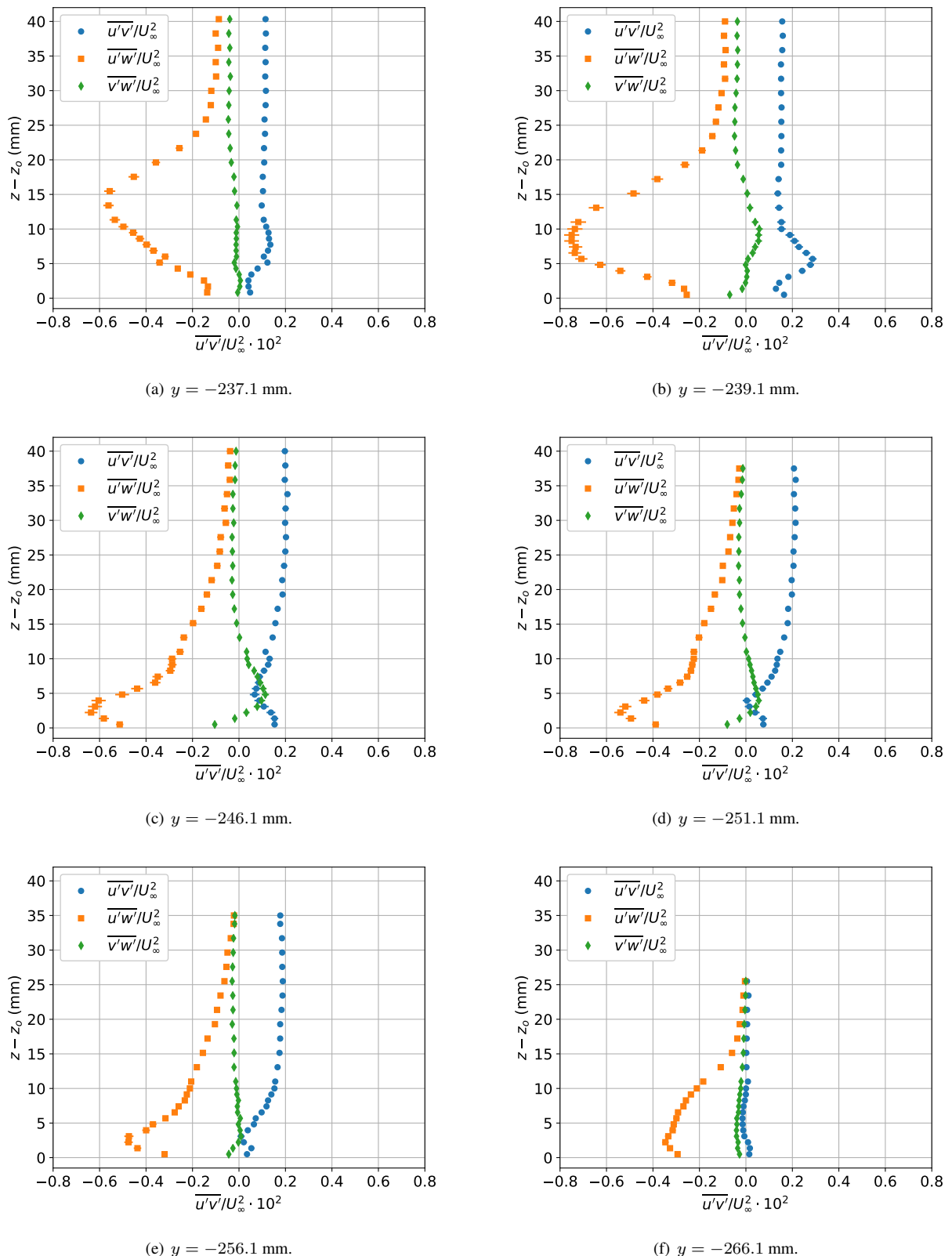


Figure 27. Reynolds shear-stress profiles in the corner-flow region of the F6 wing with leading-edge extension at $x = 2892.6 \text{ mm}$ and $\alpha = 5^\circ$.

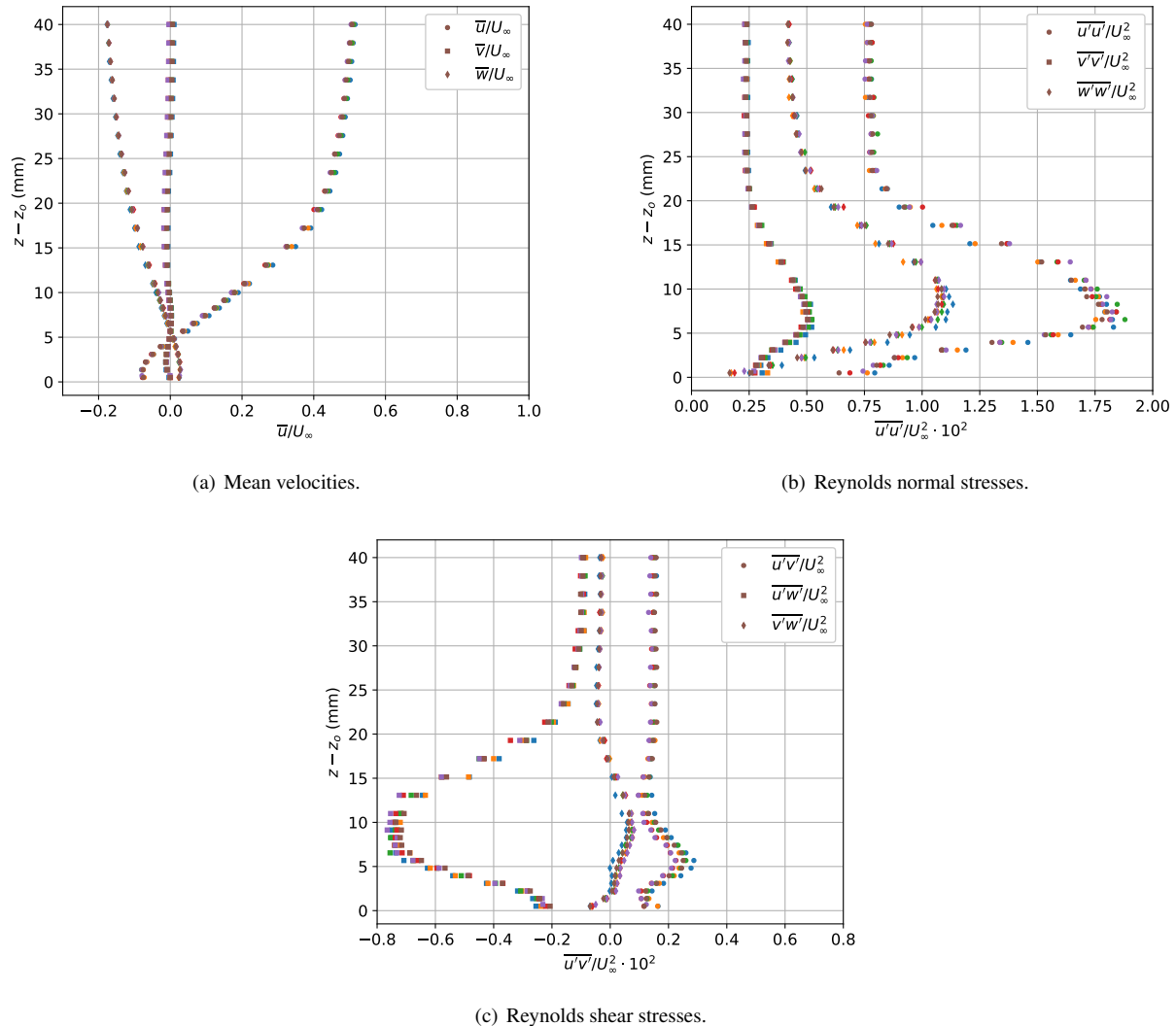


Figure 28. Repeat LDV profile measurements at $x = 2892.6$ mm, $y = -239.1$ mm for the F6 wing with leading-edge extension at a model pitch angle of $\alpha = 5^\circ$.

D. Unsteady Pressure Results

In this section, we present a few sample results from the unsteady pressure measurements on the F6 wing with leading-edge extension. For that case, unsteady pressures were collected for model pitch angles ranging from -7.5° to 10° in 2.5° increments. Broadband RMS pressures for sensors located near the trailing-edge corner of the starboard wing are shown in Fig. 30. For a given model pitch angle, each symbol marks the (x, y) location of the sensor and the color represents the broadband RMS pressure. The symbol for the sensor located at $x = 2866.92$ mm, $y = 244.81$ mm is missing because that sensor was damaged at some point during the installation into the wing. For several pitch angles, the sensor symbols are overlaid on a corresponding image of the oil-flow visualization (obtained on the port side of the model and mirror imaged) to provide a spatial reference. The fuselage surface is located at $y = 236.1$ mm and the wing trailing edge is located at $x = 2961.9$ mm. As the model pitch angle is increased, the corner-flow separation moves upstream and expands outboard along the wing span to envelope an increasingly larger number of pressure sensors. As that occurs, the broadband RMS pressure for sensors within the separated-flow region increases and it continues to increase up to the largest model pitch angle that was tested.

The power spectral densities (PSD) of the unsteady pressures for several model pitch angles are shown in Fig. 31 for two sensor locations on the starboard F6 wing with leading-edge extension. Included in the plots are the wind-off PSD to show the sensor noise floor. The broad peak in the PSDs at about $f = 16.6$ kHz is present in both the wind-off and wind-on spectra and does not appear to be a flow-induced characteristic; rather, it is believed to be a characteristic

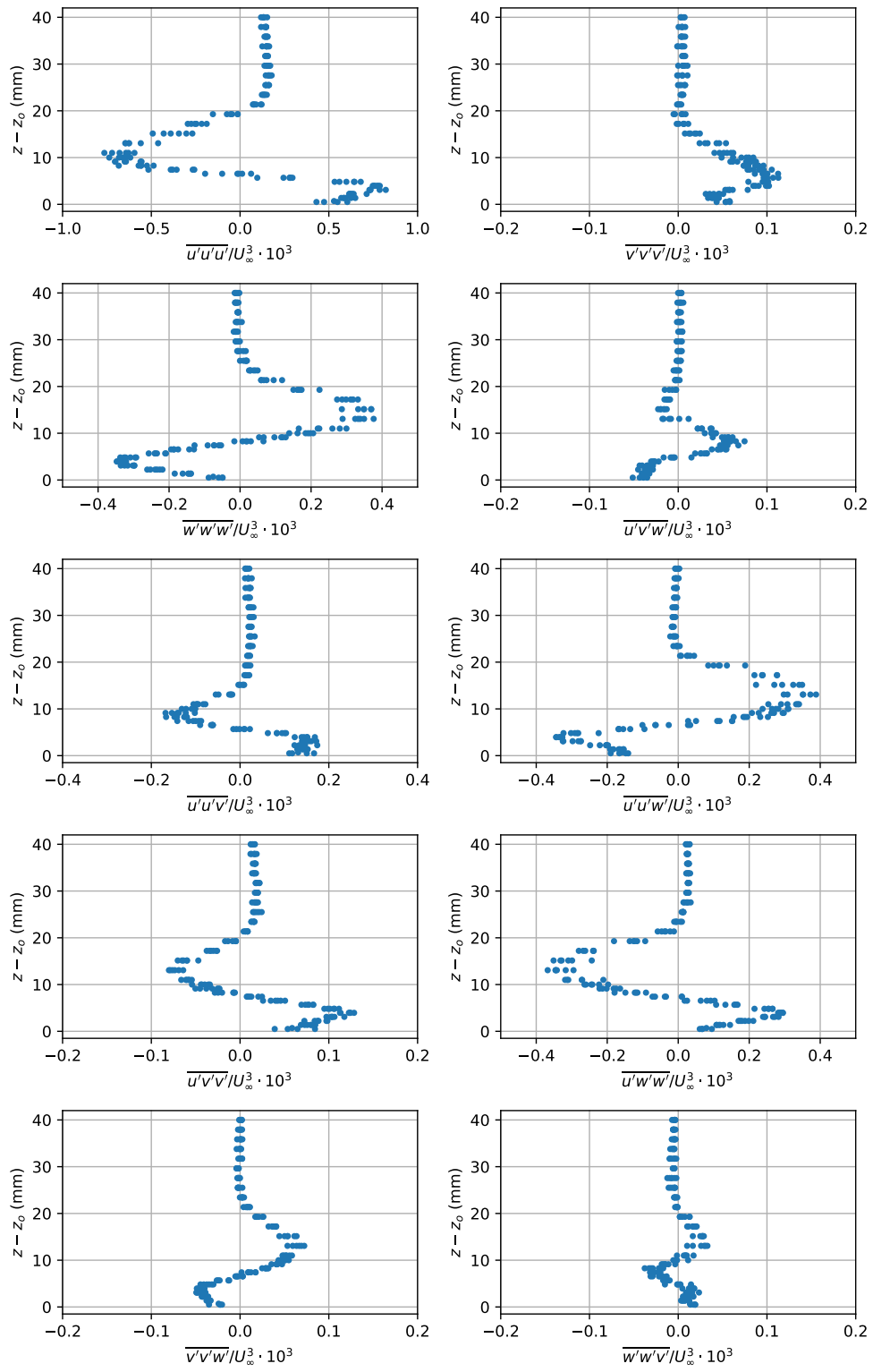


Figure 29. Triple-product profiles at $x = 2892.6$ mm, $y = -239.1$ mm for the F6 wing with leading-edge extension at a model pitch angle of $\alpha = 5^\circ$.

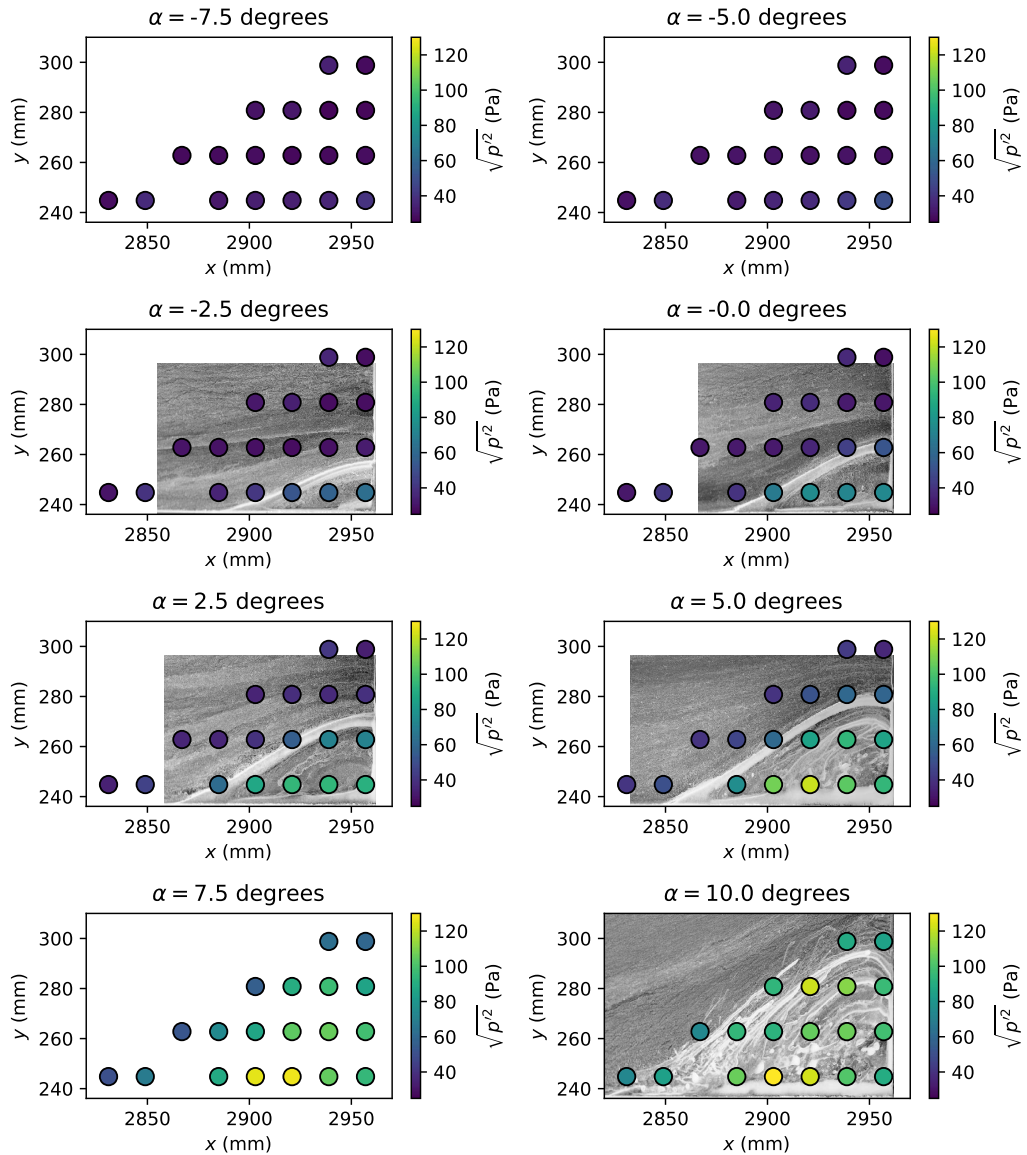


Figure 30. Broadband RMS pressures in the trailing-edge region of the starboard F6 wing with leading-edge extension versus model pitch angle. For each subplot, the symbols denote the (x, y) -locations of the unsteady pressure sensors and they are color coded according to the broadband RMS pressure. In specific cases, the RMS pressures are overlaid on an oil-flow visualization (mirror-imaged from the port wing of the model) for spatial reference.

of the in-line amplifier of the unsteady pressure transducers. In fact, all of the sensors on the model have a similar preamplifier and display a similar spectral peak. The sensor located at $x = 2902.94$ mm, $y = 244.81$ mm (Fig. 31a) is near the middle of the first streamwise row of sensors, closest to the fuselage surface. Here, the PSDs are nearly the same for pitch angles up to -5° and for these pitch angles, the sensor lies upstream of the corner-flow separation. As we move to larger model pitch angles, the corner-flow separation sweeps past the sensor and there is an increase in the spectral energy and a shift in spectral content towards progressively lower frequencies. The sensor located at $x = 2956.94$ mm, $y = 262.79$ mm is at the end of the second streamwise row of sensors and is near the trailing edge of the wing. As with the other sensor, the PSDs are nearly the same for pitch angles up to -5° and after that, the PSDs display broadband energy growth—primarily at lower frequencies—as the separated-flow region moves outboard over the sensor. There is also some shift in the spectral content towards lower frequencies with increasing model pitch angle.

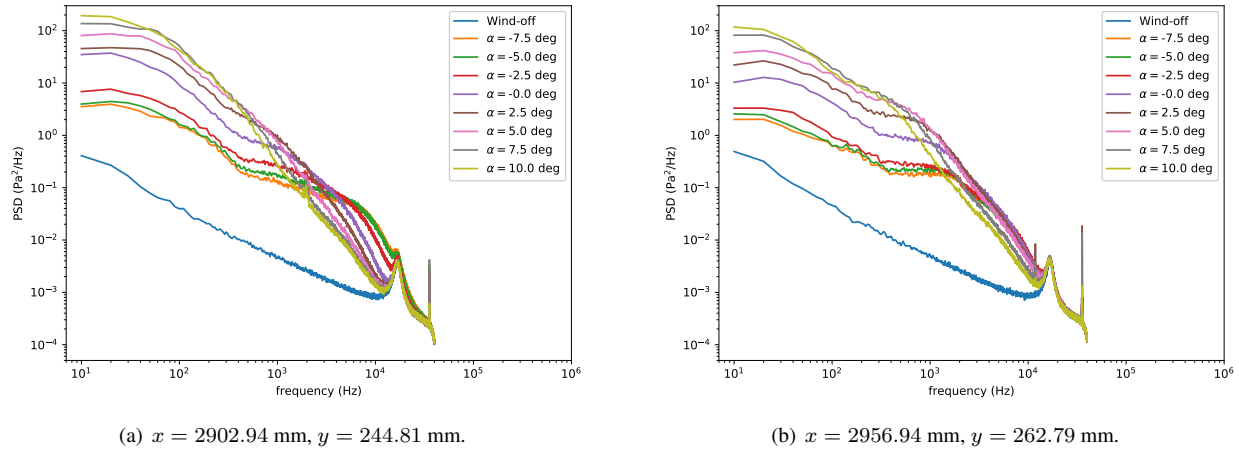


Figure 31. Power spectral densities of the unsteady pressures versus model pitch angle at two locations on the starboard F6 wing with leading-edge extension.

IV. Summary

In this paper, we have provided an initial report out on the results of a recent CFD validation experiment on a full-span wing-fuselage junction model. This model geometry—which was designed in coordination with CFD subject matter experts from government, industry, and academia—exhibits a separated corner-flow region near the wing trailing edge that current RANS models are unable to reliably predict. The ultimate goal of this experimental effort is to provide a publicly-available high-quality flow field and surface data set with quantified boundary conditions, geometry, and measurement uncertainties. It is expected that this data set will be suitable for use in CFD workshop environments and will help CFD practitioners validate and improve their predictive capabilities for turbulent separated corner flows.

The primary objective of this first test entry with the junction model was to perform flow-field measurements with internally mounted laser Doppler velocimetry (LDV) systems. The flow-field measurements were focused in three regions on the port side of the junction model: 1) the boundary layer on the fuselage, well upstream of the wing leading edge; 2) the boundary layer in the vicinity of the wing leading edge; and 3) the corner-flow region near the wing trailing edge. For the corner-flow region in particular, profile measurements were acquired upstream of the corner-flow separation, near the beginning of separation, and within the separated-flow region. All three components of mean velocity and all six independent components of the Reynolds-stress tensor were calculated from the LDV measurements. In addition, all ten independent triple products of the velocity components were calculated. Sample results for these flow-field measurements were presented and the general features associated with them were discussed. Sample infrared images were presented to show the natural and tripped states of the boundary layer on the junction model. Oil-flow visualizations of the wing trailing edge region showed the progressive growth in the corner-flow separation with increasing model pitch angle and measurements of the length and width of the separated-flow region were presented. Finally, sample results from the unsteady pressure measurements in the trailing edge corner region of the starboard wing were presented and discussed.

In future work, additional analysis of the LDV and unsteady pressure results is planned, including detailed uncertainty quantification. A second test entry with the junction model is also scheduled for late 2019 and there, we plan additional flow-field measurements with both particle image velocimetry (PIV) and LDV. It is expected that the PIV measurements will help identify regions of interest in the flow field where more detailed LDV profiles can be acquired. Both techniques will also provide data at the same locations in the flow field and that will further aid the uncertainty quantification for the experimental measurements.

Acknowledgements

This work was supported by the NASA Transformational Tools and Technologies (TTT) project of the Transformative Aerodynamics Concepts Program. The authors thank all members of the Juncture Flow Team for their dedication and insights throughout the course of this effort. The authors would also like to thank the staff of the 14- by 22-Foot Subsonic Tunnel for their support during the test entry—their dedication was a key contributor to our success.

References

- ¹Vassberg, J. C., Tinoco, E. N., Mani, M., Brodersen, O. P., Eisfeld, B., Wahls, R. A., Morrison, J. H., Zickuhr, T., Laflin, K. R., and Mavriplis, D. J., "Abridged Summary of the Third AIAA Computational Fluid Dynamics Drag Prediction Workshop," *Journal of Aircraft*, Vol. 45, No. 3, May–June 2008, pp. 781–798.
- ²Rumsey, C. L., Neuhart, D. H., and Kegerise, M. A., "The NASA Juncture Flow Experiment: Goals, Progress, and Preliminary Testing (Invited)," AIAA Paper 2016-1557, January 2016.
- ³Rumsey, C. L. and Morrison, J. H., "Goals and Status of the NASA Juncture Flow Experiment," AVT Specialists Meeting on Progress and Challenges in Validation Testing for CFD, STO-MP-AVT-246-03, September 2016.
- ⁴Aeschliman, D. P. and Oberkampf, W. L., "Experimental Methodology for Computational Fluid Dynamics Code Validation," *AIAA Journal*, Vol. 36, No. 5, May 1998.
- ⁵Rhode, M. N. and Oberkampf, W. L., "Estimation of Uncertainties for a Model Validation Experiment in a Wind Tunnel," *Journal of Spacecraft and Rockets*, Vol. 54, No. 1, January–February 2017.
- ⁶Kuester, M. S., Borgoltz, A., and Devenport, W. J., "Experimental Visualization of Juncture Separation Bubbles at Low- to Moderate-Reynolds Numbers," AIAA Paper 2016-3880, June 2016.
- ⁷Kegerise, M. A. and Neuhart, D. H., "Wind Tunnel Test of a Risk-Reduction Wing/Fuselage Model to Examine Juncture-Flow Phenomena," NASA TM 219348, 2016.
- ⁸Rumsey, C. L., Carlson, J. R., Hannon, J. A., Jenkins, L. N., Bartram, S. M., Pulliam, T. H., and Lee, H. C., "Boundary Condition Study for the Juncture Flow Experiment in the NASA Langley 14x22-Foot Subsonic Wind Tunnel," AIAA Paper 2017-4126, June 2017.
- ⁹Neuhart, D. H. and McGinley, C. B., "Free-Stream Turbulence Intensity in the Langley 14- by 22-Foot Subsonic Tunnel," NASA TP 213247, 2004.
- ¹⁰Gentry, G. L., Quinto, F. P., Gatlin, G. G., and Applin, Z. T., "The Langley 14- by 22-Foot Subsonic Tunnel," NASA TP 3008, 1990.
- ¹¹Boney, A. D., "Data Reduction Functions for the Langley 14- by 22-Foot Subsonic Tunnel," NASA TM 218513, 2014.
- ¹²Albrecht, H. E., Borys, M., Damaschke, N., and Tropea, C., *Laser Doppler and Phase Doppler Measurement Techniques*, Springer, Berlin, Germany, 2003.
- ¹³Miles, P. C., "Geometry of the Fringe Field Formed in the Intersection of Two Gaussian Beams," *Applied Optics*, Vol. 35, No. 30, October 1996, pp. 5887–5895.
- ¹⁴Lowe, K. T., *Design and Application of a Novel Laser-Doppler Velocimeter for Turbulence Structural Measurements in Turbulent Boundary Layers*, Ph.D. thesis, Virginia Polytechnic Institute and State University, 2006.
- ¹⁵Lowe, K. T. and Simpson, R. L., "An Advanced Laser-Doppler Velocimeter for Full-Vector Particle Position and Velocity Measurements," *Meas. Sci. Technol.*, Vol. 20, 2009, pp. 1–16.
- ¹⁶Brooks, D. R. and Lowe, K. T., "Development and Application of a Compact Spatially Resolving Vector Laser Velocimeter for Near Surface Flow Measurements," *16th Int. Symp. on Applications of Laser Techniques to Fluid Mechanics*, Lisbon, Portugal, 2012.
- ¹⁷Lowe, K. T., Byun, G., Neuhart, D. H., and Simpson, R. L., "Auto-Calibration of Spatially-Resolving Laser-Doppler Velocimeters," AIAA Paper 2013-0044, January 2013.
- ¹⁸Kegerise, M. A. and Neuhart, D. H., "An Experimental Investigation of a Wing-Fuselage Junction Model in the NASA Langley 14- by 22-Foot Subsonic Wind Tunnel," NASA TM in preparation.
- ¹⁹Ölgmen, S. M. and Simpson, R. L., "An Experimental Study of a Three-Dimensional Pressure-Driven Turbulent Boundary Layer," *Journal of Fluid Mechanics*, Vol. 290, 1995, pp. 225–262.
- ²⁰Hurst, A. M., Olsen, T. R., Goodman, S., VanDeWeert, J., and Shang, T., "An Experimental Frequency Response Characterization of MEMS Piezoresistive Pressure Transducers," ASME Paper GT2014-27159, June 2014.
- ²¹Braslow, A. L., Hicks, R. M., and Harris, R. V., "Use of Grit-Type Boundary-Layer-Transition Trips on Wind-Tunnel Models," NASA TN D-3579, September 1966.
- ²²Braslow, A. L. and Knox, E. C., "Simplified Method for Determination of Critical Height of Distributed Roughness Particles for Boundary-Layer Transition at Mach Numbers from 0 to 5," NASA TN 4363, September 1958.